THE GEOLOGICAL SOCIETY OF AMERICA®

# Chronology, stable isotopes, and glaciochemistry of perennial ice in Strickler Cavern, Idaho, USA

**Jeffrey S. Munroe†, Samuel S. O'Keefe, and Andrew L. Gorin**
*Geology Department, Middlebury College, Middlebury, Vermont 05753, USA*

## ABSTRACT

**Cave ice is an understudied component of the cryosphere that offers potentially significant paleoclimate information for midlatitude locations. This study investigated a recently discovered cave ice deposit in Strickler Cavern, located in the Lost River Range of Idaho, United States. Field and laboratory analyses were combined to determine the origin of the ice, to limit its age, to measure and interpret the stable isotope compositions (O and H) of the ice, and to investigate its glaciochemistry. Results indicate that the ice forms through snow densification, freezing of infiltrating water, and refreezing of meltwater. Radiocarbon dating revealed that an ~30-m-thick deposit of layered ice and organic matter accumulated over the past several centuries. In contrast, a 3.5-m-tall ice stalagmite began forming almost 2000 yr ago. Stable isotopes in the stalagmite and in the layered ice generally have slopes that parallel the local winter meteoric water line; however, $\delta^{18}O$ and $\delta^{2}H$ values are offset to the right of this line, indicating the influence of sublimation. Values of $\delta^{18}O$ are lower in older ice, signaling cooler temperatures during the Little Ice Age. Calcium is the most abundant element in the ice, followed by Na, Mg, and K. Principal component analyses revealed a group of elements related to the local bedrock, a second group reflecting regional transport of mineral dust, and a third group suggestive of eolian transport from a mining dust source. Future work should build upon this foundation to further exploit the significant paleoenvironmental information archived in Strickler Cavern.**

## INTRODUCTION

The past several decades have witnessed a massive increase in research attention focused on the cryosphere. Work that began in Antarctica during the first International Geophysical Year in the late 1950s (e.g., Summerhayes, 2008), increasingly collaborative efforts to extract long ice cores from Antarctica (e.g., Jouzel et al., 2007; Petit et al., 1999) and Greenland (e.g., Grootes et al., 1993), satellite-based monitoring of glaciers (e.g., Wahr et al., 2000) and sea-ice extent (e.g., Serreze et al., 2007), field and laboratory investigations of ice-rich permafrost (e.g., Romanovsky et al., 2010; Schirrmeister et al., 2013), and coordinated monitoring of alpine glacier mass balances (e.g., Haeberli et al., 2000) are all examples of cryosphere-centric research that have revealed tremendous information about the operation of Earth's climate system and paleoclimatic variability during the Quaternary. Despite these successes, a notable drawback of this research is its uneven spatial distribution: Because most features of the modern cryosphere are located in the polar regions or at high elevations, lower-latitude and lower-altitude areas are typically underrepresented.

Subterranean accumulations of perennial ice in caves, hereafter "cave ice," are less-studied components of the cryosphere that offer a potential solution to this problem. Caves containing perennial ice have been reported from a wide variety of locations around the globe (Kern and Perşoiu, 2013). Significantly, they are often found in midlatitudes at elevations below alpine glaciers and in locations where ice-rich permafrost or other cryospheric archives are absent (Perşoiu and Onac, 2012). In light of this potential, researchers have begun to focus on cave ice as a source of paleoclimate information (Laursen, 2010). Cave ice formed from precipitation that infiltrates the ground carries a paleoenvironmental signal in stable isotopes of hydrogen and oxygen (Yonge and MacDonald, 1999). Geochemical variability in successive layers of cave ice can provide a record of past changes in atmospheric circulation (Kern et al., 2011a). Alternating intervals of ice accumulation and ablation provide evidence of fluctuations in winter snowfall and summer temperature over time (e.g., Luetscher et al., 2005; Stoffel et al., 2009), and changes in cave ice mass balances observed through long-term monitoring have been linked to weather patterns (Schöner et al., 2011; Colucci et al., 2016). Pollen and other botanical evidence incorporated in the ice can provide information about changes in surface environments (Feurdean et al., 2011). Cave ice sequences can be dated with radiocarbon, tritium, dendrochronology, and other techniques (e.g., Luetscher et al., 2007; Kern et al., 2009; Spötl et al., 2014), allowing paleoenvironmental data to be studied as time series. Initial results from these efforts have been promising (e.g., Kern et al., 2011a; Perşoiu et al., 2011), but there is also cause for concern, because many cave ice deposits are rapidly disappearing (e.g., Fuhrmann, 2007; Kern and Perşoiu, 2013; Pflitsch et al., 2016). This situation has added new urgency to the investigation of cave ice and has motivated a call for increased collaborative study of these deposits before they are lost forever (Veni et al., 2014).

Caves containing perennial ice have been most intensively studied in the Alps and in eastern Europe; in contrast, cave ice has received relatively little attention in North America. Many sites were mentioned in a seminal work by the naturalist Edwin Balch over 100 yr ago, which described ice caves all over the world and speculated on their origins (Balch, 1900). More recently published North American work includes long-term monitoring of ice in Candelaria Cave, New Mexico (Dickfoss et al., 1997), in Merrill Cave on the California-Oregon border (Fuhrmann, 2007), at Lava Beds National Monument in California (Kern and Thomas, 2014), and in a lava tube on the Big Island of Hawaii (Pflitsch et al., 2016). Ice caves have also been studied at a number of locations

†jmunroe@middlebury.edu

*GSA Bulletin*; January/February 2018; v. 130; no. 1/2; p. 175–192; https://doi.org/10.1130/B31776.1; 12 figures; 4 tables; published online 29 August 2017.

in the northern Rocky Mountains (Marshall and Brown, 1974; Lauriol and Clark, 1993; MacDonald, 1994; Yonge and MacDonald, 1999; Yonge, 2014). These projects have reinforced the notion that cave ice is a significant paleoclimate archive, but that potential remains profoundly underdeveloped.

Here, we report on our study of a recently discovered cave ice deposit at a moderate elevation (~2500 m) in midlatitude (~44°N) in Idaho, United States. Previous reconnaissance work and mapping indicated that the ice deposit is in excess of 30 m thick and possibly several hundred years old (Cecil et al., 2004). These characteristics, coupled with the dearth of cave ice studies from this region, the absence of glaciers from this part of the Rocky Mountains, and concerns about the stability of cave ice under a warming climate, motivated a field- and laboratory-based investigation in pursuit of the following objectives:

(1) to investigate the origin of the ice present in the cave;

(2) to determine the age of the ice;

(3) to evaluate the potential paleoclimate significance of stable isotope variations in the ice; and

(4) to analyze and interpret the glaciochemistry of the ice.

## SETTING

This research focused on perennial ice in Strickler Cavern, a solution cave in the Lost River Range of Idaho, United States (Fig. 1). This fault-bounded mountain range is composed primarily of Paleozoic carbonate and mudstone units separated by unconformities (Wilson and Skipp, 1994). Maximum summit elevations reach in excess of 3800 m, with ~2000 m of relief relative to the adjacent valley floors. The central part of the Lost River Range exhibits classic alpine glacial geomorphology (Foster et al., 2008), although no active glaciers remain, and the Pleistocene glacial record has not been formally studied.

Strickler Cavern is located at an elevation of ~2500 m above sea level (asl) on land managed by the U.S. Department of Agriculture Salmon-Challis National Forest. As required by the U.S. Forest Service as a condition for working in Strickler Cavern, the specific location of the cave is withheld to protect this unique and vulnerable resource. The cave formed in the Devonian-age Grand View Dolomite, which dips to the SW (Mapel et al., 1965). These rocks feature medium to thick bedding, are finely crystalline, and are dull gray in color. The hillside surrounding the cave entrance is forested with Douglas fir (Pseudotsuga menziesii). Climatic data are not available for the cave site; however, data collected since 1978 at the Mill Creek Summit SNOTEL (Snowpack Telemetry) station at a slightly higher elevation (2680 m) in the Salmon River Mountains NW of the Lost River Range are likely similar. The mean annual air temperature at the Mill Creek Summit SNOTEL is 1.1 °C. December through February temperatures average −7.1 °C, whereas June through August temperatures average 10.7 °C. Mean annual precipitation is 730 mm, with less than 20% of the precipitation falling during the summer months. December and January have the greatest precipitation (>12% of the annual total in each month), and 64% of the annual precipitation falls during months with subzero average air temperatures (November through April).

Strickler Cavern can be classified as a "static cave with congelation ice and firn" (Luetscher and Jeannin, 2004, Fig. 1, p. 64). The air circulation within the cave is likely static because the only entrance is at the top, and cold air that enters through density settling in winter is trapped in the cave during the summer. This permits the year-round maintenance of subzero cave temperatures despite a mean annual air temperature >0 °C at the surface.

The entrance to Strickler Cavern is a collapse doline, ~5 m in diameter, that descends ~8 m to the top of a steep-sided cone of snow, firn, and ice ~5 m tall (Fig. 2). This "snow cone" rises from a relatively flat floor of ice that forms the Upper Level of the cave (Fig. 1). During July of 2015, a shallow (<10 cm) meltwater pond covering ~25 m$^2$ was located on the floor of the Upper Level to the north of the snow cone. From the Upper Level, a nearly vertical slope of ice leads down into a large chamber known as the Big Room (Fig. 1). This room, with a ceiling height locally in excess of 15 m, features a floor of ice that grades laterally into a slope of breakdown derived from the cave roof. Packrat middens, wood, and other organic debris are scattered across this slope, and an inaccessible dome extends upward in the center of the ceiling. A large stalagmite of ice occupies the center of the Big Room floor, and a smaller stalagmite is located on the breakdown slope.

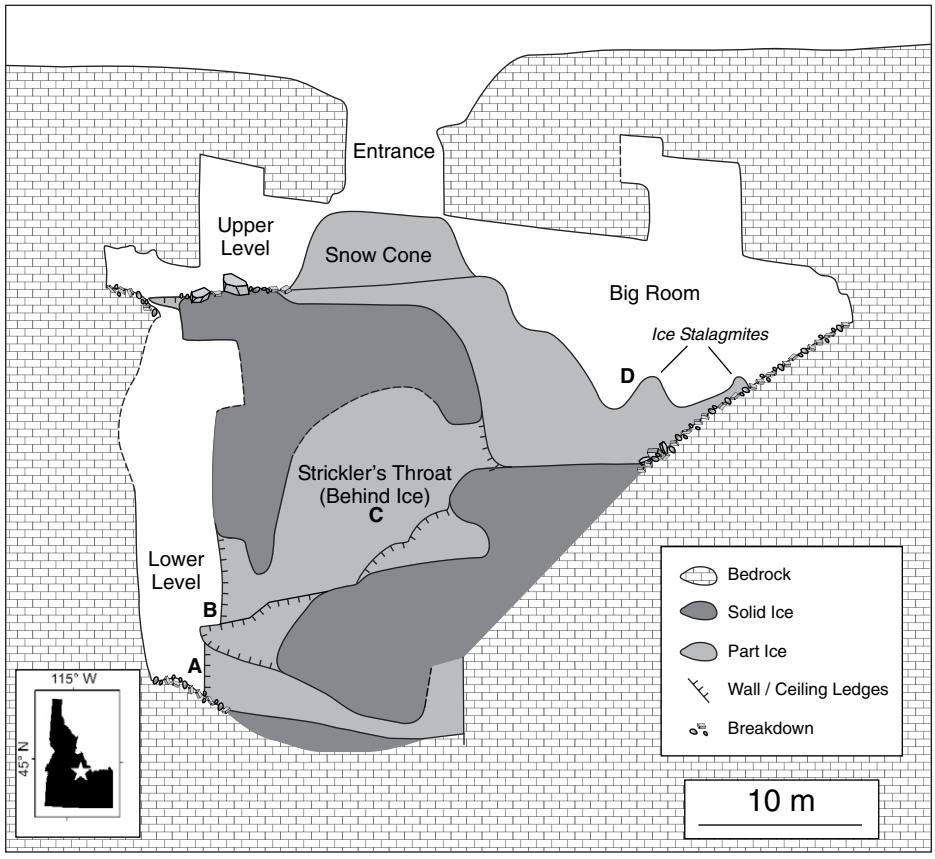


**Figure 1. Vertical profile map of Strickler Cavern (adapted from digital mapping provided by David Herron, U.S. Department of Agriculture, U.S. Forest Service). A–D denote the positions of the four studied exposures. Exposure E was excavated into the snow cone below the entrance (Fig. 2). Inset shows the location of the cave within the state of Idaho, United States.**

Air temperature in the Big Room was stable at 0 °C during field investigations. From the north side of the Big Room, a narrow passage known as Strickler's Throat leads downward between the cave wall and the ice (Fig. 1). This passage provides access to the Lower Level of the cave, where an exposure of ice extends upward for more than 20 m. The deepest accessible part of the cave is reached ~40 m below the ground surface, although the depth of the base of the ice deposit is unknown. Groundwater flux to the cave is negligible, and no carbonate speleothems were observed.

## METHODS

Field work was conducted in Strickler Cavern over 5 d in July 2015. The vertical entrance was rigged with static ropes for ascending and descending. A third rope was configured with a pulley system for raising and lowering equipment and samples. A thorough reconnaissance was first conducted in all accessible levels of the cave to identify ice exposures suitable for more detailed investigation. Criteria considered in this evaluation included accessibility, safety, exposure extent, presence of organic material for radiocarbon dating, and evidence of folding, distortion, or melt unconformities in the ice. This approach revealed four exposures considered optimal for subsequent study, designated A–D, along with the snow cone (exposure E) beneath the entrance doline. All exposures were measured, photographed, and described. Samples for radiocarbon dating were collected with a focus on the largest, least-decomposed organic fragments. Samples of ice for stable isotope and glaciochemical analysis were extracted with a 13-cm-long hand screw. To eliminate the potential for contamination by water films on the ice surface, the first ~5 cm section was discarded, and only the deeper ice was retained. Most samples targeted the center of individual ice layers; however, in exposures A, B, and C, a suite of samples spanning a single layer was also taken to check for intralayer trends in stable isotope values. All ice samples were extruded from the screw into 50 mL tubes and capped for transport to the surface. After melting overnight, each sample was transferred to a 15 mL tube, filled to the top with no headspace, and capped tightly.

In total, 26 samples of organic matter were radiocarbon dated at the University of California–Irvine. Samples were subjected to standard preparatory steps, including an acid-base-acid wash, graphitized, and analyzed by Accelerator Mass Spectrometry (AMS) (https://www.ess.uci.edu/group/ams/protocols). Resulting radiocarbon ages were calibrated in Oxcal 4.2 (Ramsey, 2009) using the IntCal13 calibration curve (Reimer et al., 2013). Bayesian statistics within Oxcal were utilized to refine the age estimates for sequences of samples with known stratigraphic context.

Measurements of $\delta^{18}O$ and $\delta^{2}H$ were performed at the Stable Isotope Laboratory of Stefan cel Mare University, Suceava, Romania, using a Picarro L2130i cavity ring-down spectroscopy (CRDS) analyzer coupled to a high-precision vaporizer. Melted ice samples were stored at 4 °C and passed through a 0.22 µm filter to remove particulates before analysis. Each sample was manually injected at least nine times, and the average of the last four injections was used, once the standard deviation was below 0.03 for $\delta^{18}O$ and 0.3 for $\delta^{2}H$. The results were normalized to the Vienna standard mean ocean water–standard light Antarctic precipitation (VSMOW-SLAP) scale and reported in per mil against VSMOW, with precision better than ±0.03‰ for $\delta^{18}O$ and ±0.3‰ for $\delta^{2}H$.

Elemental abundances in ice samples were measured with a Thermo Fisher iCAP Qc inductively coupled plasma–mass spectrometer (ICP-MS) at Middlebury College, Middlebury, Vermont. Each sample was run in triplicate, with blanks and standards between every five analyses. Standards included NIST SRM 1643f (trace elements in water) at regular concentration and as a 1:10 dilution, along with in-house multi-element standards for major and most trace elements. Results were drift corrected, the root mean square (RMS) error was calculated for repeat analyses to confirm consistency, and triplicates were averaged. Further analysis focused on elements with abundances above detection limits of 1.0 ppb. Detection limits were determined through analysis of diluted standards and cross-checked by duplicate ICP-MS analyses at the Vermont Department of Environmental Conservation.

Stable isotope and glaciochemical results were compared between ice types using a Mann-Whitney test (two independent samples) and Kruskal-Wallis test (>2 independent samples). Nonparametric tests were utilized given the unequal number of samples representing the different ice types, the relatively small size of the data set, and the nonnormal distributions of some results. Principal component analysis (PCA) was employed to simplify the glaciochemistry data set. The PCA was conducted using a direct oblimin rotation with Kaiser normalization, and coefficients <0.3 were disregarded. Nearly identical results were obtained using a varimax rotation. All statistical analyses were conducted in IBM SPSS v24.0.

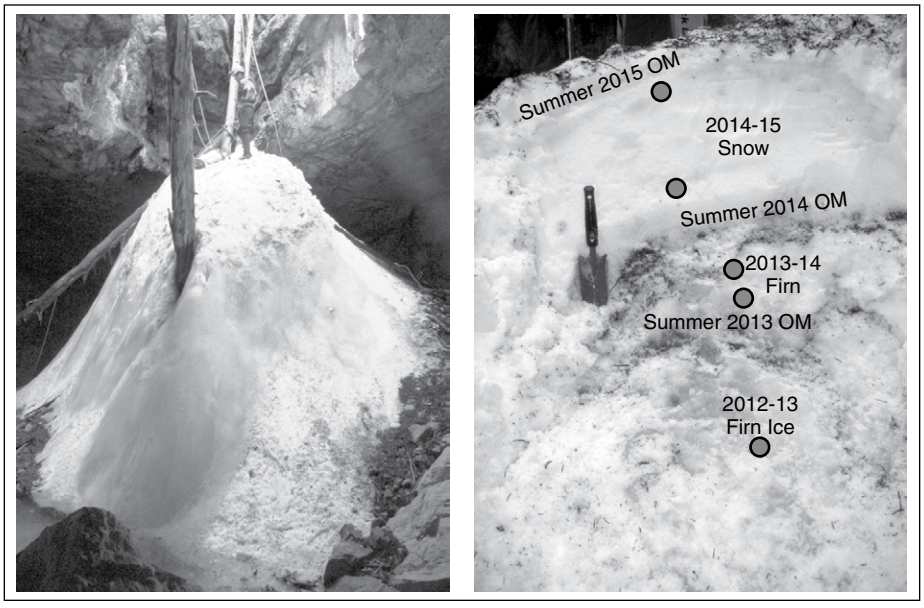


**Figure 2. (Left) Photograph of the snow cone at the base of the entrance shaft into Strickler Cavern. Note the figure on top of the cone for scale. (Right) Vertical face of the excavation into the upper part of the snow cone. The concentration of organic matter (OM) marking summer 2015 is clearly visible overlying clean snow from the 2014–2015 winter. The organic matter concentration from the previous summer (2014) is also seen overlying a layer of firn representing snow that accumulated during the 2013–2014 winter. A third layer of organic matter denotes summer 2013 and overlies denser firn that fell as snow during the 2012–2013 winter. Locations of five samples are denoted by the circles. The trowel for scale is 20 cm long.**

## RESULTS AND DISCUSSION

### Exposures

Five exposures within Strickler Cavern were studied and sampled intensively (Fig. 1), exposures A–E: they are described separately next.

#### *Exposure A*

This vertical, 4-m-tall exposure is located in the deepest part of the cave (Figs. 1 and 3). Three samples were collected for $^{14}C$ dating, along with ~1 L of bulk organic matter. Three separate layers near the base of the exposure were sampled with an ice screw. In addition, a single relatively thick layer near the center of the exposure was sampled from bottom to top with a set of six ice-screw samples.

#### *Exposure B*

This vertical, 3-m-tall exposure is located at the base of a tall (>20 m) wall of ice and organic matter (Figs. 1 and 4). Individual layers of ice and intercalated organics slope from the upper-right to lower-left, and the overall abundance of organic matter decreases from right to left. These layers are in angularity unconformity with a unit of ice devoid of organic matter at the base of the exposure. Samples for radiocarbon dating were collected at the bottom and top of the exposure, with a third ~1 L sample of bulk organic matter collected from an open dilation crack. Sixteen ice samples were collected from individual layers, and five more were collected from a single layer near the top of the exposure. Finally, three ice samples were collected from organic-free ice to the right of the exposure, adjacent to the wall of the cave.

#### *Exposure C*

The samples representing exposure C were collected along a vertical transect through Strickler's Throat (Fig. 1). Three organic samples for radiocarbon dating were collected from the bottom, middle, and top of the exposure over a vertical span of ~10 m. Seven ice samples were drilled from a single, 15-cm-thick layer of organic-free ice near the location of the middle organic sample.

#### *Exposure D*

Exposure D consists of two separate exposures that collectively provide a window into the internal stratigraphy of the large ice stalagmite on the floor of the Big Room (Figs. 1 and 5). The lower exposure on the north side of the stalagmite measured ~1.5 × 1 m and revealed several distinct layers of ice and clastic mineral debris in angular unconformity with one another (Fig. 5). Sixteen ice samples were drilled from these layers, and four samples of organic matter were collected. The upper exposure, on the west side of the stalagmite, covered ~1 × 1 m and revealed the internal stratigraphy of the upper part of the stalagmite. Eleven ice samples were collected from this exposure, and eight stratigraphically higher samples were collected by drilling directly into the stalagmite surface. Finally, four samples of organic matter were collected from the upper exposure.

#### *Exposure E*

This exposure was excavated with a shovel into the snow cone beneath the cave entrance (Figs. 1 and 2). The surface of the snow featured a concentration of organic debris overlying ~60 cm of clean snow. Beneath this snow, there was a second concentration of organic matter, with a denser layer of firn ~30 cm thick beneath it. A third layer of organic matter marked the transition to an ice-rich layer that was difficult to excavate by hand. Two samples were taken from the uppermost snow layer, two from the firn layer, and a fifth from the top of the deepest, most ice-rich layer. Finally, a single sample of organic matter for radiocarbon dating was collected from the ice forming the floor of the Upper Room near the wall where a small fissure provided access to deeper stratigraphy.

### Origins of the Ice

In an attempt to standardize ice cave nomenclature, Luetscher and Jeannin (2004) noted that at least seven different types of ice have been reported from caves. The two most common origins are (1) recrystallization of snow, and (2) freezing of infiltrating water (Luetscher and Jeannin, 2004). Both of these processes are operating in Strickler Cavern, where snow falling into the entrance constitutes the major ice input. Exposure E clearly reveals that recently fallen snow at the top of the cone in the entrance shaft transitions progressively downward into firn and solid ice (Fig. 2). Given the surrounding climate, snow accumulates in the cave entrance during the winter. Conversely, organic matter primarily accumulates on top of the snow during the summer. As each winter's residual snow is buried the following year, the snow is compressed to firn and eventually ice with intercalated concentrations of organic matter (e.g., Luetscher, 2013). This "firn ice" comprises a large, but unknown, fraction of the central ice deposit in the cave. Disturbance events in the forest surrounding the cave entrance could deliver pulses of organic matter during the winter, complicating this stratigraphy. Yet to a first order, the individual couplets of ice and organic matter represent seasonal components of annual accumulation, analogous to varves in a lacustrine

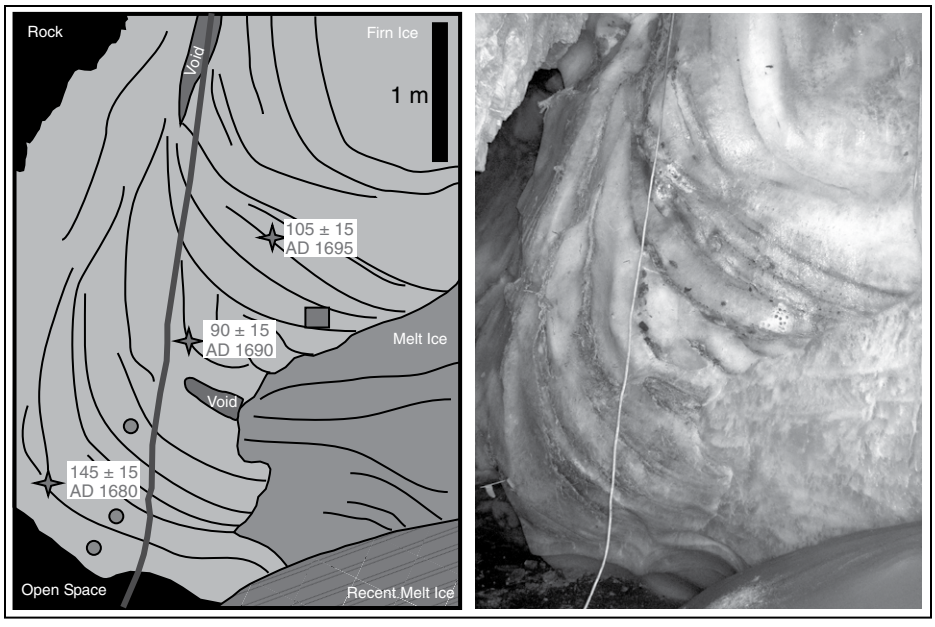


**Figure 3. (Left) Tracing of exposure A showing major types of ice, prominent layers, and locations of samples. Circles denote samples from individual layers, whereas the square identifies the location where a single layer was sampled with a series of contiguous samples. Three radiocarbon ages are also shown (yr B.P.), along with their corresponding calibrated ages derived from a Bayesian analysis. (Right) Photograph of exposure A. The vertical line is a rope.**

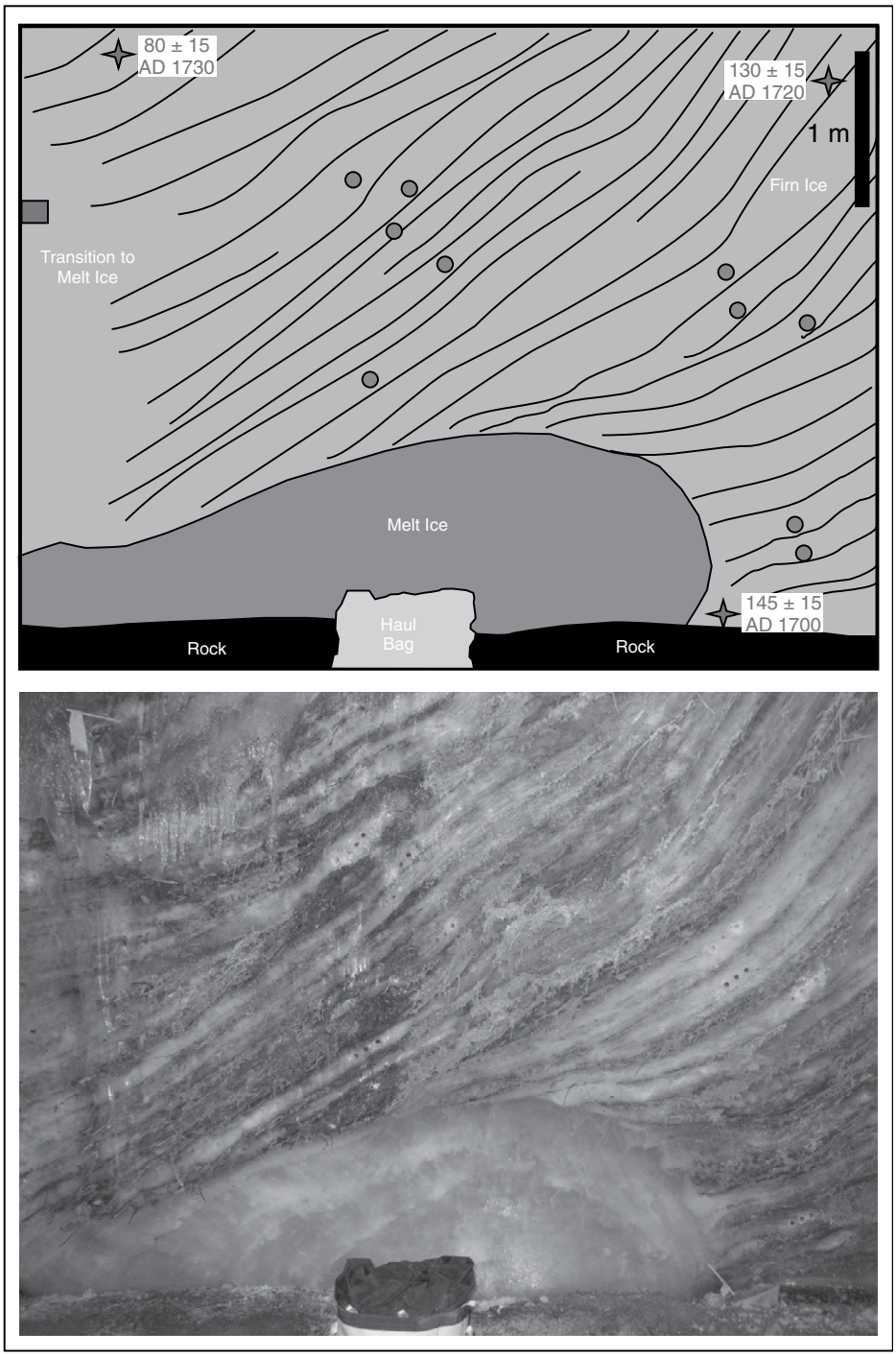


**Figure 4. (Top) Tracing of exposure B showing major types of ice, prominent layers, and locations of samples. Circles denote samples from individual layers, whereas the square identifies the location where a single layer was sampled with a series of contiguous samples. Three radiocarbon ages are also shown (yr B.P.), along with their corresponding calibrated ages derived from a Bayesian analysis. (Bottom) Photograph of exposure B. Note the contorted layers, the angular unconformity with the underlying melt ice body, and the overall decrease in organic matter content from right to left. Not all sample locations are visible in the photograph.**

system. Stresses operating on this ice upon deeper burial lead to plastic deformation, yielding folding patterns visible in deeper exposures (Figs. 3 and 4).

The central ice mass also contains a distinct type of translucent ice in relatively thick layers that is commonly devoid of organic matter. This ice is present, for example, on the lower right side of exposure A (Fig. 3), at the base of exposure B (Fig. 4), along the cave wall to the right of exposure B, and in Strickler's Throat. This ice is interpreted as "melt ice" produced through the refreezing of meltwater, for instance, in the pond that forms seasonally where sunlight hits the floor of the Upper Room. Meltwater from this pond may also drain laterally, freezing as it descends into the Big Room (Fig. 1), and creating melt ice overlying a core of firn ice. The general lack of organic matter in melt ice is attributable to its formation away from the snow cone where the organic matter enters the cave. The close proximity of the snow cone and the adjacent meltwater pond may explain how the organic matter content of ice layers can change horizontally, as noted at exposure B (Fig. 4).

A third type of ice forms from the freezing of dripwater that infiltrates the cave ceiling. This "congelation ice," which forms the stalagmite sampled at exposure D (Figs. 1 and 5), is transparent, is generally devoid of organic matter, and is associated with thin coatings of white cryogenic precipitates (Žák et al., 2008). Unconformities visible within the stalagmite under transmitted light (Fig. 5) reflect episodes of melting possibly triggered by changes in air currents or the position of the drip point on the cave ceiling. The relatively infrequent occurrences of organic matter in congelation ice are generally restricted to these unconformities, likely reflecting the improbability of organic fragments accumulating on the convex stalagmite surface.

The mechanisms of ice genesis inferred for Strickler Cavern are consistent with those proposed for other well-studied ice caves in the literature. Firn ice has been reported from caves in the Canadian Rocky Mountains (MacDonald, 1994), and the Alps (Stoffel et al., 2009; Spötl et al., 2014), but it has not previously been identified in the United States. Ice formed through in situ freezing of small volumes of liquid water is common in caves from a wide variety of locations. Some of this ice is derived from thin films of seepage water, analogous to the congelation ice forming the stalagmite in this study. For instance, bodies of layered ice in Candelaria Cave, New Mexico (Dickfoss et al., 1997), in various caves of the Canadian Rockies (Marshall and Brown, 1974; Yonge and MacDonald, 1999; Yonge, 2014), in the Monlesi Cave, Switzerland (Luetscher et al., 2007), and in the

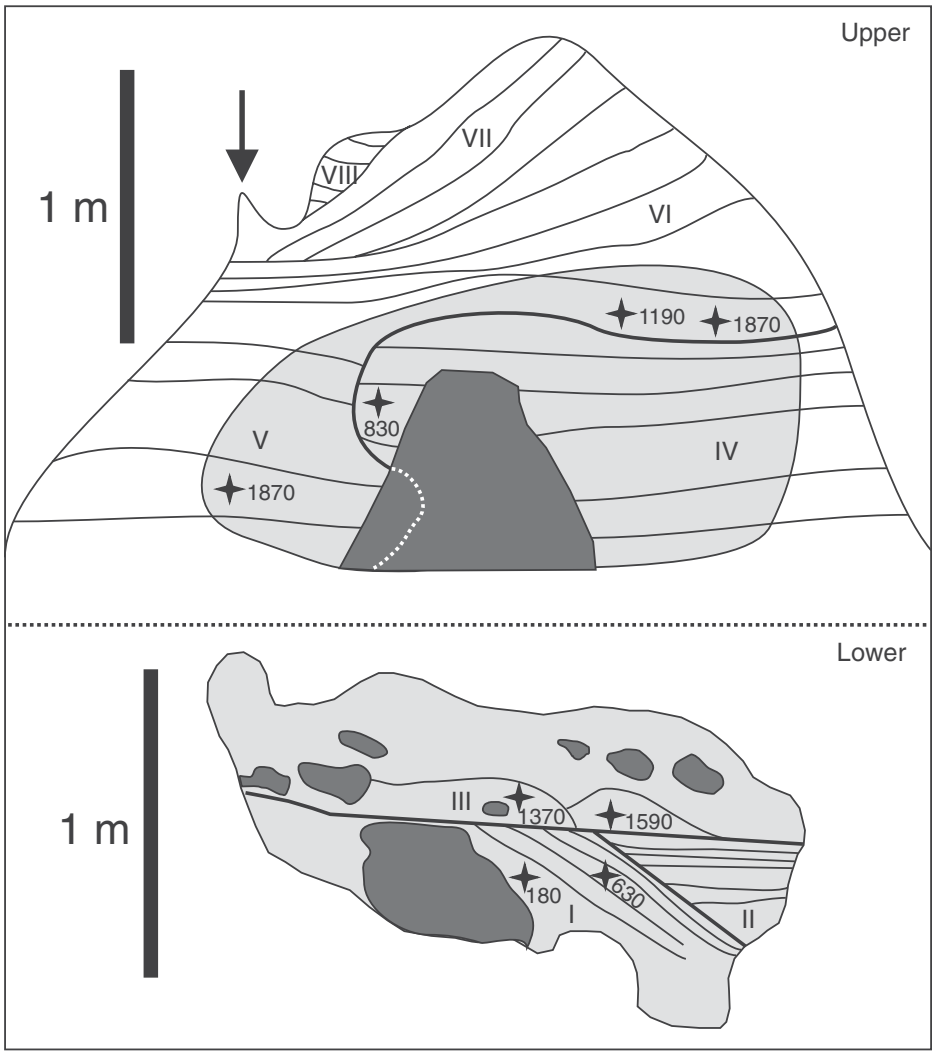


**Figure 5. Schematic of the lower and upper exposures (gray shading) into the stalagmite comprising exposure D. In the upper part of the transparent stalagmite, layers and unconformities were visible in transmitted light; however, the exact spatial relationship between these two exposures is unknown. Roman numbers identify individual packages of concordant layers (see Fig. 9). Dark-gray shapes denote prominent rocks. Stars mark the locations of radiocarbon samples, which are presented as calibrated ages in years A.D. The dotted white line marks the inferred continuation of a prominent melt unconformity in the upper part of the stalagmite. The black arrow designates the active drip location where a finger of ice rises from the overall stalagmite mound.**

Eisriesenwelt Cave (May et al., 2011) and Mammuthöhle, Austria (Kern et al., 2011a), are composed of congelation ice. Refreezing of thicker water layers to form melt ice has also been presented in the literature; for instance, ice forming from ponded water was noted in Merrill Cave, California (Fuhrmann, 2007), and in Scărişoara Cave, Romania (Perşoiu et al., 2011). Similarly, ice formed when meltwater produced near the warmer entrance of a cave migrates deeper into the colder parts of a cave system has been noted in many studies, including Vukušic Cave in Croatia (Kern et al., 2011b). Many studies have also noted more than one type of ice in a given cave (e.g., Luetscher and Jeannin, 2004; Spötl et al., 2014), and so the co-occurrence of three different types of ice in Strickler Cavern is not unusual.

## Age of the Ice

### *Radiocarbon Results*

The age of the ice in Strickler Cavern was assessed by radiocarbon dating of 26 samples of organic matter collected from the three exposures of layered ice, the snow cone, and the stalagmite (Table 1). Dated material included sticks, conifer cone scales, charcoal, packrat scat, and deciduous leaves. All samples from the layered ice deposit have radiocarbon ages between 85 ± 15 and 240 ± 15 yr B.P. When calibrated, these results yield multiple possible age ranges (as many as five separate ranges for some samples), generally corresponding to death dates from the late seventeenth century through to the mid-twentieth century (Table 1). Organic matter from the deeper parts of the stalagmite yielded older ages, as discussed below.

### *Interpretation of Radiocarbon Results from the Layered Ice*

Interpretation of these ages requires consideration of factors that could induce offsets between the measured radiocarbon age of organic fragments and the true age of the enclosing ice. Because the organic matter was produced outside of the cave environment, there is the possibility of a lag time between the death of the organic matter and the time at which it was deposited in the cave (e.g., Spötl et al., 2014). For instance, a conifer cone could detach from a tree and be stored on the forest floor before transport into the cave. This situation would result in a radiocarbon age that is older than the actual age of the enclosing ice. This possibility cannot be ruled out for these samples; however, it is unlikely that the magnitude of this offset would be more than a decade. Organic debris would decompose fairly rapidly in the litter layer on the forest floor surrounding the cave. Yet, the generally small, delicate organic fragments selected for dating showed little evidence of decomposition, suggesting that they were transported into the cave soon after they detached from their source. Furthermore, the steep slope above the cave makes it unlikely that small, mobile organic fragments would linger on the forest floor for long before rolling into the cave entrance. Short-term storage of organic matter as standing dead wood or on the forest floor before deposition could explain the scatter observed in the radiocarbon ages (Table 1) determined for subsamples from the bulk material collected at exposure A (SIC-18, SIC-19, and SIC-20) and exposure B (SIC-21, SIC-22, and SIC-23). Nonetheless, the calibration ranges for these radiocarbon ages overlap, meaning that possible differences in the duration of storage before deposition are small relative to their overall radiocarbon ages.

At the other extreme, vertically oriented openings within the layered ice deposit could allow organic matter to fall down inside the ice body, yielding radiocarbon ages that are younger than the true age of the enclosing ice. This process

TABLE 1. RADIOCARBON RESULTS FROM STRICKLER CAVERN

| UCIAMS no. | Sample ID | Exposure | Material | Fraction modern | ± | $\delta^{14}C$ (‰) | ± (‰) | $^{14}C$ age (yr B.P.) | ± (yr) | Median (yr A.D.) | 2σ range (probability) (yr A.D.) | Midpoint* (yr A.D.) | Considered in Bayesian model |
|---|---|---|---|---|---|---|---|---|---|---|---|---|---|
| 168135 | SIC-1 | E | Stick | 0.9894 | 0.0014 | –10.6 | 1.4 | 85 | 15 | 1850 | 1695–1728 (26.3%), 1812–1854 (23.3%), 1867–1919 (45.8%) | 1890 | X |
| 168136 | SIC-2 | A | Cone scales | 0.9821 | 0.0014 | –17.9 | 1.4 | 145 | 15 | 1780 | 1672–1698 (15.3%), 1725–1778 (33.9%), 1797–1815 (11.6%), 1834–1878 (14.3%), 1916–1943 (20.3%) | 1750 | X |
| 168137 | SIC-3 | A | Stick | 0.9887 | 0.0018 | –11.3 | 1.8 | 90 | 15 | 1840 | 1694–1728 (27.7%), 1812–1854 (26.0%), 1866–1919 (41.7%) | 1890 | X |
| 168138 | SIC-4 | A | Cone scales | 0.9868 | 0.0016 | –13.2 | 1.6 | 105 | 15 | 1840 | 1690–1730 (27.4%), 1810–1895 (56.5%), 1902–1924 (11.6%) | 1850 | X |
| 168139 | SIC-5 | B | Stick | 0.9819 | 0.0015 | –18.1 | 1.5 | 145 | 15 | 1780 | 1672–1698 (15.3%), 1725–1778 (33.9%), 1797–1815 (11.6%), 1834–1878 (14.3%), 1916–1943 (20.3%) | 1750 | X |
| 168140 | SIC-6 | B | Cone scales | 0.9903 | 0.0014 | –9.7 | 1.4 | 80 | 15 | 1880 | 1696–1726 (24.5%), 1813–1836 (17.5%), 1844–1852 (2.1%), 1876–1918 (51.3%) | 1900 | X |
| 168141 | SIC-7 | C | Stick | 0.9792 | 0.0013 | –20.8 | 1.3 | 170 | 15 | 1760 | 1666–1685 (16.8%), 1731–1784 (50.8%), 1796–1808 (9.7%), 1926–... (18.1%) | 1760 | X |
| 168142 | SIC-8 | C | Stick | 0.9803 | 0.0013 | –19.7 | 1.3 | 160 | 15 | 1760 | 1667–1691 (15.6%), 1728–1782 (50.9%), 1796–1811 (11.3), 1922–1946 (17.6%) | 1760 | X |
| 168143 | SIC-9 | C | Salix leaf | 0.9844 | 0.0068 | –15.6 | 6.8 | 130 | 60 | 1810 | 1666–1784 (40.1%), 1796–… (55.3%) | 1890 | X |
| 168144 | SIC-10 | D | Stick | 0.7968 | 0.0011 | –203.2 | 1.1 | 1825 | 15 | 180 | 134–234 (95.4) | 180 | |
| 168145 | SIC-11 | D | Stick | 0.8368 | 0.0013 | –163.2 | 1.3 | 1430 | 15 | 630 | 600–650 (95.4%) | 630 | |
| 168146 | SIC-12 | D | Stick | 0.9225 | 0.0013 | –77.5 | 1.3 | 650 | 15 | 1360 | 1285–1316 (40.0%), 1355–1390 (55.4%) | 1370 | |
| 168147 | SIC-13 | D | Stick | 0.9573 | 0.0014 | –42.7 | 1.4 | 350 | 15 | 1560 | 1470–1525 (43.6%), 1556–1632 (51.8%) | 1590 | |
| 168148 | SIC-14 | D | Stick | 0.9879 | 0.0014 | –12.1 | 1.4 | 100 | 15 | 1840 | 1692–1729 (27.8%), 1810–1920 (67.6%) | 1870 | |
| 168149 | SIC-15 | D | Stick | 0.8601 | 0.0012 | –139.9 | 1.2 | 1210 | 15 | 820 | 768–882 (95.4%) | 830 | |
| 168150 | SIC-16 | D | Scat | 0.9892 | 0.0019 | –10.8 | 1.9 | 85 | 20 | 1850 | 1694–1728 (25.5%), 1812–1919 (69.9%) | 1870 | |
| 168151 | SIC-17 | D | Charcoal | 0.8983 | 0.0014 | –101.7 | 1.4 | 860 | 15 | 1190 | 1160–1218 (95.4%) | 1190 | |
| 168152 | SIC-18 | A | Stick | 0.9880 | 0.0014 | –12.0 | 1.4 | 95 | 15 | 1850 | 1694–1728 (27.6%), 1812–1919 (67.7%) | 1870 | |
| 168153 | SIC-19 | A | Stick | 0.9703 | 0.0014 | –29.7 | 1.4 | 240 | 15 | 1790 | 1646–1667 (73.5%), 1783–1796 (21.9%) | 1660 | |
| 168154 | SIC-20 | A | Stick | 0.9814 | 0.0015 | –18.6 | 1.5 | 150 | 15 | 1760 | 1668–1696 (15.2%), 1726–1780 (40.6%), 1796–1814 (11.8%), 1836–1877 (7.7%), 1916–1944 (20.0%) | 1760 | |
| 168155 | SIC-21 | B | Stick | 0.9807 | 0.0015 | –19.3 | 1.5 | 155 | 15 | 1760 | 1668–1694 (15.7%), 1726–1782 (48.0%), 1796–1814 (12.2%), 1918–1945 (19.6%) | 1760 | |
| 168156 | SIC-22 | B | Stick | 0.9782 | 0.0015 | –21.8 | 1.5 | 175 | 15 | 1770 | 1666–1684 (18.1%), 1734–1784 (49.4%), 1796–1807 (8.8%), 1928–… (19.1%) | 1760 | |
| 168157 | SIC-23 | B | Stick | 0.9839 | 0.0015 | –16.1 | 1.5 | 130 | 15 | 1840 | 1680–1710 (16.1%), 1716–1739 (11.2%), 1745–1764 (3.5%), 1802–1890 (48.7%), 1909–1938 (15.9%) | 1850 | X |
| 168158 | SIC-24 | C | Stick | 0.9818 | 0.0016 | –18.2 | 1.6 | 150 | 15 | 1760 | 1668–1696 (15.2%), 1726–1780 (40.6%), 1796–1814 (11.8%), 1836–1877 (7.7%), 1916–1944 (20.0%) | 1750 | |
| 168159 | SIC-25 | C | Stick | 0.9889 | 0.0015 | –11.1 | 1.5 | 90 | 15 | 1840 | 1694–1728 (27.7%), 1812–1854 (26.0%), 1866–1919 (41.7%) | 1890 | |
| 168160 | SIC-26 | C | Stick | 0.9855 | 0.0015 | –14.5 | 1.5 | 115 | 15 | 1840 | 1686–1730 (26.3%), 1808–1892 (58.4%), 1908–1927 (10.7%) | 1850 | |

*Note*: UCIAMS—University of California Irvine Accelerator Mass Spectrometry Laboratory.
*Midpoint of calibration range with maximum probability, rounded to nearest 10 yr.

may be happening in Strickler's Throat, where the ice has locally melted back from the cave wall. If so, this could explain the varied ages obtained for individual sticks removed from the bulk organic sample at exposure C (SIC-24, SIC-25, and SIC-26) that was collected from loose material (Table 1). In this case, the true age of the ice at the base of exposure C is likely represented by sample SIC-7 (170 ± 15 yr B.P.), because the organic fragments dated from the loose bulk sample at this depth are all slightly younger than the ages for the stratigraphically higher middle (SIC-8, 160 ± 15 yr B.P.) and upper (SIC-9, 130 ± 15 yr B.P.) samples from this exposure (Table 1). Nonetheless, given that vertically oriented openings penetrating the layered ice deposit were not observed beyond this one location, and that it would be difficult for voids to remain open in the face of infiltrating meltwater and ductile flow of the ice, it is unlikely that the transport of younger organic matter into the interior of the ice deposit is a widespread process.

### *Bayesian Analysis of Layered Ice Results*

Because the samples collected from the layered ice deposit are relatively close in age and have death dates that fall in a complicated section of the radiocarbon calibration curve, further analysis was necessary to refine their most probable age estimates. Given that the stratigraphic relationships between many samples are known, a Bayesian approach was employed to narrow the most probable calibration ranges for the samples considered to provide the tightest constraint on the actual ages of the ice layers enclosing them. Samples selected for this Bayesian analysis are identified in Table 1, and the results of this analysis are presented in Table 2 and Figure 6. Samples were selected from the bottom, middle, and top of exposures A, B, and C, as well as from the floor of the Upper Room. Where multiple samples existed for a given position, the sample exhibiting the least evidence for decomposition or reworking was used. Samples with radiocarbon ages stratigraphically inconsistent with the ages of overlying/underlying samples were discarded (for instance, those from the loose bulk sample collected from the base of exposure C in Strickler's Throat). Finally, a sample ("Mitch") collected by a previous study (Cecil et al., 2004) from an unspecified location below exposure A was also included in the Bayesian analysis. For the purpose of plotting, model ages were assigned to each sample after consideration of the Bayesian results (Table 2). Most model ages are the midpoint of the most probable calibration range. However, in a few cases, these midpoints were shifted slightly to better align with peak of calibration probability.

TABLE 2. BAYESIAN MODEL AGES

| Sample no. | Sample ID | Exposure | $^{14}$C age (yr B.P.) | ± (yr) | Modelled 2σ range (probability) (yr A.D.) | Model age (yr A.D.) |
|---|---|---|---|---|---|---|
| 168135 | SIC-1 | E | 85 | 15 | 1810–1920 (95.4%) | 1900 |
| 168143 | SIC-9 | C | 130 | 60 | 1760–1910 (95.4%) | 1850 |
| 168142 | SIC-8 | C | 160 | 15 | 1730–1820 (72.8%), 1840–1880 (22.6%) | 1800 |
| 168141 | SIC-7 | C | 170 | 15 | 1720–1780 (72.2%), 1830–1870 (23.2%) | 1750 |
| 168140 | SIC-6 | B | 80 | 15 | 1700–1740 (73.6%), 1810–1850 (21.9%) | 1730 |
| 168157 | SIC-23 | B | 130 | 15 | 1690–1740 (75.1%), 1750–1770 (2.2%), 1800–1850 (18.1%) | 1720 |
| 168139 | SIC-5 | B | 145 | 15 | 1680–1770 (92.5%), 1800–1820 (2.9%) | 1700 |
| 168138 | SIC-4 | A | 105 | 15 | 1680–1730 (95.4%) | 1695 |
| 168137 | SIC-3 | A | 90 | 15 | 1680–1720 (95.4%) | 1690 |
| 168136 | SIC-2 | A | 145 | 15 | 1670–1700 (95.4%) | 1680 |
| Beta-173904 | Mitch | * | 280 | 70 | 1450–1670 (95.4%) | 1560 |

*From the deepest accessible part of the cave, below exposure A.

This approach greatly narrowed the probable calibration ranges of the 10 selected radiocarbon dates (Table 2) and suggests that the layered ice deposit accumulated between ca. A.D. 1560 and A.D. 1900 (Fig. 6). Given these results, exposure A accumulated in the late 1600s, exposure B over ~30 yr in the early 1700s, exposure C between A.D. 1750 and A.D. 1850, and the ice forming the floor of the Upper Room around A.D. 1900. Because a vertical distance of ~30 m separates the uppermost (SIC-1) and lowermost (Mitch) samples (Table 2), the 340 yr difference between their model ages suggests an overall ice accumulation rate of ~9 cm/yr. This estimate is consistent with the observed thickness of firn ice layers between the organic matter concentrations thought to represent summer ablation seasons. It is important to note that unrecognized folding or overturning within the ice could render this Bayesian approach invalid, along with the mechanisms discussed earlier that could yield offsets between radiocarbon ages and true ice ages. Nonetheless, with these caveats in mind, the most salient point of this analysis is that the layered ice deposit within Strickler Cavern appears to have accumulated over the last four centuries. This ice, therefore, may contain a high-resolution, perhaps annually resolved, record of snowfall and climate over the last several hundred years in this part of the Rocky Mountains.

### *Ages from the Stalagmite*

Seven samples were radiocarbon dated from the stalagmite (exposure D) composed of congelation ice that is separate from the main layered ice body (Fig. 5; Table 1). These samples yielded many older ages, including 1825 ± 15 yr B.P. for the stratigraphically lowest sample (SIC-10) and 1430 ± 15 yr B.P. for the next higher sample (SIC-11). When calibrated, these ages indicate that the ice forming the base of the stalagmite began accumulating 1500–2000 yr ago (Table 1). The two youngest ages are from the upper exposure (Fig. 5). Sample SIC-14 yielded an age of 100 ± 15 yr B.P., and SIC-16 returned 85 ± 15 yr B.P. The maximum probability calibrated age range for both these samples is between A.D. 1810 and 1920. Notably, sample SIC-16 was a collection of packrat scat from the same layer as charcoal fragments (SIC-17) that returned a much older age of 860 ± 15 yr B.P. The scat and charcoal were incorporated in a clastic-rich layer ~4 cm thick. Previous studies have interpreted assemblages of organics with divergent ages in the same layer as evidence of a melting episode that eliminated an unknown thickness of ice, concentrating organic matter and rubble as a lag marking an unconformity (e.g., Spötl et al., 2014). Applying this logic here leads to the conclusion that a significant melting event sometime after A.D. 1850 eliminated much of the ice that accumulated between ca. A.D. 1200 and 1850. The dates of A.D. 1360 and A.D. 1560 from the rubbly layer at the top of the lower exposure (Fig. 5) might also reflect this melting event, although the direct stratigraphic relationship between the two exposures is unclear. Melting after A.D. 1850 could be attributable to the end of the Little Ice Age (Grove, 2004), although it is not clear how that climatic transition would have resulted in an increase in cave temperature. One possibility is that increased snowfall and/or cooler summer temperatures during the peak of the Little Ice Age allowed the snow cone to grow upward until it sealed the base of the entrance doline (Fig. 1). Sealing this opening, or at least constricting it dramatically, would exclude cold winter air from the cave, resulting in rising cave temperatures due to geothermal heating. This theory cannot be tested with the available evidence, but it is an intriguing possibility for explaining how sections of the stalagmite could have been lost to ablation. Parts of the firn ice deposit may also have melted at this time, possibly resulting in the carapace of melt ice that covers the slopes leading from the Upper Level to the Big Room.

Whatever the explanation for the melt unconformity in the upper part of the stalagmite, accumulation of congelation ice clearly resumed after the end of the Little Ice Age. Approximately 1 m of ice overlies the unconformity that yielded the youngest radiocarbon age, and a delicate, upward-pointing "finger" of ice atop the stalagmite mound represents the location of actively freezing drips (Fig. 5). Angular unconformities separating packages of concordant layers visible within the upper part of the stalagmite (Fig. 5) suggest that the specific locations where drips emerge from the cave ceiling have changed repeatedly in the <150 yr since ice accumulation resumed.

### *Radiocarbon Summary and Significance*

Radiocarbon dating reveals that the firn ice in Strickler Cavern accumulated over the past four centuries, whereas the stalagmite composed of congelation ice contains a discontinuous record extending back nearly 2000 yr. The 26 radiocarbon ages supporting these conclusions represent a major increase in the number of numerical age estimates available for subterranean ice deposits in North America. Before this work, the most thoroughly dated ice cave in the United States was Candelaria Cave in New Mexico (Dickfoss et al., 1997). The ice in this cave accumulates through the freezing of seepage water (Dickfoss et al., 1997), forming congelation ice analogous to the stalagmite in Strickler Cavern. Four AMS ages were reported on organic fragments from Candelaria Cave, and four additional ages were measured on $CO_2$ extracted from the ice itself. The gas ages were dismissed by Dickfoss et al. (1997) because their $\delta^{13}C$ values were too low (<–17‰); however, two "unidentified twig" samples from near the base of the ~4-m-thick ice deposit yielded ages of 3116 ± 77 and 1819 ± 100 yr B.P. When calibrated, these ages correspond to 1540–1190 B.C. (median of 1370 B.C.) and 40 B.C. to A.D. 420 (median of A.D. 200). Two samples from higher in the layered ice deposit yielded younger ages of 243 ± 55 yr B.P. (calibrated median of A.D. 1660) and 27 ± 73 yr B.P. (calibrated median of A.D. 1840), suggesting a hiatus between deposition of the lower and upper sections of the ice body.

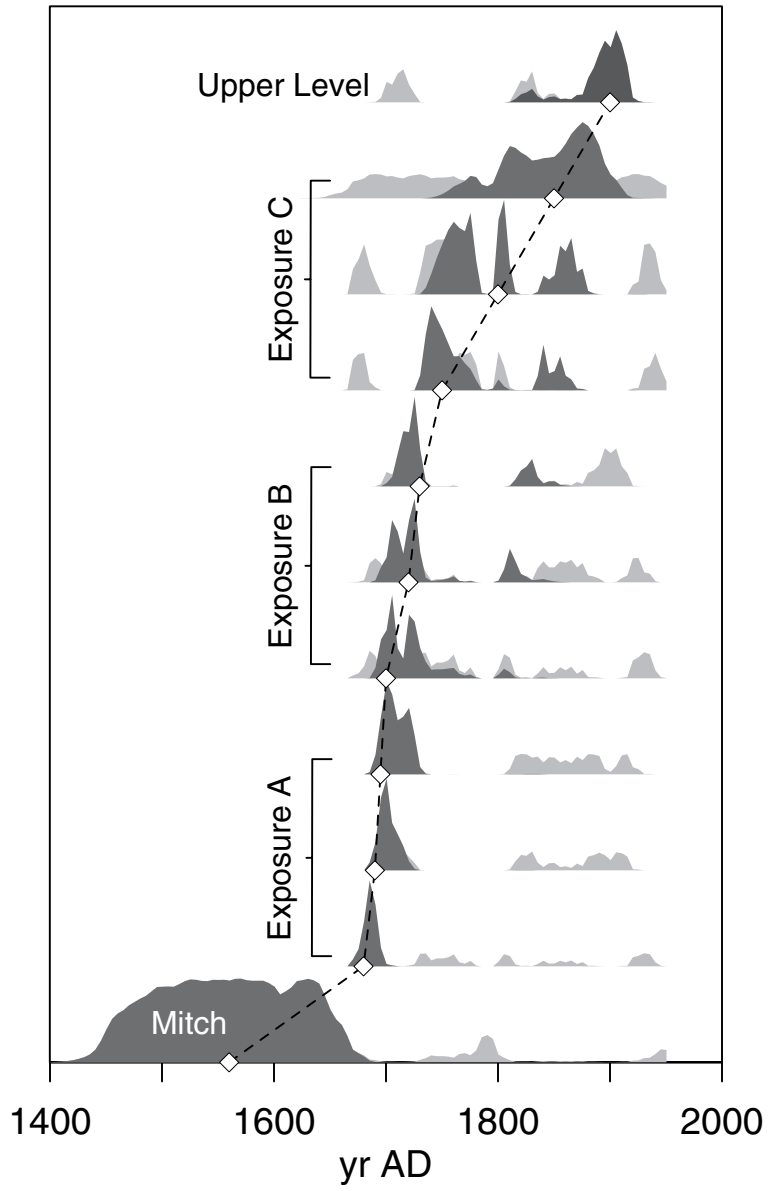


**Figure 6. Results of the Bayesian analysis of 11 radiocarbon dates in stratigraphic order through the firn ice body. Full calibration ranges are shown in light gray, whereas the Bayesian refined calibration ranges are shown in dark gray. White diamonds mark the inferred model ages used to assign overall ages to the ice sampled in exposures A, B, C, and in the Upper Level. The basal sample "Mitch" was reported by a previous reconnaissance study (Cecil et al., 2004).**

Beyond Candelaria Cave, a single radiocarbon age is available for Serendipity Cave at an elevation of 2175 m in the Rocky Mountains of Alberta, Canada (Yonge and MacDonald, 1999). Here, a 15-m-thick deposit of stratified ice is interpreted to result from freezing of seepage water and water vapor (MacDonald, 1994). A collection of packrat pellets from 70 cm above the base of this ice deposit yielded an age of 970 ± 80 yr B.P. (Yonge and MacDonald, 1999), which calibrates to A.D. 890–1230 (median of A.D. 1080). Dating of cryogenic cave calcite in two caves in Arctic Canada also resulted in age estimates older than ca. 1000 yr B.P. (Lauriol and Clark, 1993). Other than these examples, we are not aware of other published ages for subterranean ice in North America.

Radiocarbon dating has been more extensively employed in studies of ice caves in Europe. For example, radiocarbon dating was used in evaluating the mass balance of ice in Hundsalm Cave, Austria, over the past 1500 yr (Spötl et al., 2014). Similarly, radiocarbon dating combined with dendrochronology were used in evaluating climatic controls on the accumulation of ice over the past 1200 yr in St. Livres Cave, Switzerland (Stoffel et al., 2009).

This review emphasizes the relatively small number of studies in which numerical age constraints have been developed for cave ice deposits. The relatively old ages determined for the base of the stalagmite in Strickler Cavern are consistent with maximum ice ages reported by other published studies. However, the total number of radiocarbon ages produced in this study arguably makes Strickler Cavern one of the most thoroughly dated cave ice deposits in the world.

## Stable Isotope Results

### *Stable Isotopes in the Ice*

In total, 80 samples for analysis of stable isotopes of O and H were collected from Strickler Cavern. Nine samples were collected from exposure A, 24 from exposure B, 7 from exposure C, 5 from the snow cone, and 35 from the stalagmite (exposure D). One sample (SIC-15-47 from near the base of Exposure D) was lost in the laboratory, leaving 79 pairs of $\delta^{18}O$ and $\delta^{2}H$ results. Values of $\delta^{18}O$ range from –18.4‰ to –12.1‰, with a mean of –15.9‰ (median of –16.0‰) and a standard deviation of 1.3‰ (Table 3). Values of $\delta^{2}H$ range from –146‰ to –94.9‰, with a mean of 128.2‰ (median of –129.9‰) and a standard deviation of 9.7‰. Values of $\delta^{18}O$ and $\delta^{2}H$ are strongly correlated, with a coefficient of determination ($r^2$) of 0.969. Plotting all 79 samples as $\delta^{18}O$ versus $\delta^{2}H$ yields a slope of 7.48 and an intercept of 9.09.

### *Stable Isotopes in Single Ice Layers*

Three subsets of samples were collected to span individual layers of ice in exposures A, B, and C (Fig. 1). Results from these samples were plotted as $\delta^{18}O$ versus $\delta^{2}H$ to identify intralayer fractionation, indicating that the ice formed through freezing of a layer of liquid water. Six samples collected from a single layer in exposure A yielded a slope of 7.7 and an intercept of –3.4‰. This slope is very similar to the global meteoric water line (Craig, 1961), indicating that no melting or refreezing was involved in the formation of this layer. In contrast, five samples from a single layer in exposure B yielded a slope of 6.5 with an intercept of –26.5‰, and seven samples from a layer in exposure C yielded a slope of 6.6 and an intercept of –22.8‰. These notably lower slopes reveal that kinetic fractionation occurred during formation of these layers,

TABLE 3. BASIC STATISTICS FOR THE PRIMARY ($\delta^{18}O$ AND $\delta^{2}H$) AND SECONDARY (D-EXCESS) ISOTOPIC PARAMETERS OF ICE FROM STRICKLER CAVERN

| | | All | Snow | Firn ice | Flow ice | Congelation ice |
|---|---|---|---|---|---|---|
| | | n = 79 | n = 5 | n = 29 | n = 11 | n = 34 |
| $\delta^{18}O$ (‰) | Mean | –15.9 | –13.1 | –16.3 | –15.4 | –16.2 |
| | Median | –16.0 | –12.9 | –16.1 | –15.2 | –16.1 |
| | St dev | 1.3 | 1.1 | 0.9 | 1.1 | 1.1 |
| | Range | –12.1 to –18.3 | –12.1 to –14.9 | –14.6 to –17.8 | –14.0 to –17.6 | –13.3 to –18.3 |
| $\delta^{2}H$ (‰) | Mean | –128.2 | –103.9 | –131.1 | –124.7 | –130.4 |
| | Median | –129.9 | –102.0 | –130.2 | –122.4 | –130.6 |
| | St dev | 9.7 | 9.3 | 5.9 | 7.0 | 7.8 |
| | Range | –94.9 to –146.1 | –94.9 to –119.1 | –118.3 to –141.3 | –116.6 to –139.7 | –107.9 to –146.1 |
| d-excess (‰) | Mean | –0.9 | 1.0 | –0.8 | –1.1 | –1.2 |
| | Median | –0.9 | 0.7 | –1.0 | –0.6 | –1.2 |
| | St dev | 1.8 | 0.5 | 1.7 | 2.6 | 1.6 |
| | Range | 2.22 to –6.30 | 1.6 to 0.5 | 2.1 to –3.8 | 1.8 to –6.3 | 2.1 to –5.8 |

strongly suggesting that the ice formed through freezing of liquid water rather than through densification of snow (Jouzel and Souchez, 1982; Perşoiu et al., 2011; Souchez and Jouzel, 1984).

These intralayer results are consistent with interpretations of the types of ice present in each exposure. The ice comprising exposure A was interpreted as firn ice with intercalated organic matter, and a slope paralleling the global meteoric water line supports this interpretation. In contrast, samples from exposure C were collected from clear ice with very low organic content interpreted as melt ice. This ice likely formed as meltwater descended between the layered ice deposit and the cave wall, or through the refreezing of a seasonal meltwater pond such as the one observed on the Upper Level, producing a slope lower than the global meteoric water line. Exposure B is a hybrid: most of the exposure reveals firn ice with high organic content, yet the single-layer samples were collected from the left side of the exposure where the abundance of organic matter is markedly less (Fig. 4). This decrease from right to left suggests a lateral transition from firn ice to melt ice. The modern meltwater pond on the floor of the Upper Level is directly adjacent to the snow cone. Refreezing of this pond will result in a horizontal gradation from organic-rich firn ice to organic-poor melt ice, and the ice comprising exposure B likely formed in an analogous setting. Collectively, the results from sequential sampling through individual ice layers support the interpretation that exposure A is composed of firn ice, exposure B features a lateral gradation from firn ice to melt ice, and exposure C is dominated by melt ice.

### *Stable Isotopes Grouped by Ice Type*

Grouping the samples according to the type of ice from which they were collected reveals notable similarities and differences (Table 3; Fig. 7). The five samples collected from the snow and firn at the top of the snow cone generally had the highest $\delta^{18}O$ values (mean of –13.1‰). In contrast, mean values for the firn and congelation ice were the lowest (means of –16.3‰), with the overall lowest values recorded in the congelation ice (–18.3‰). Patterns were similar for $\delta^{2}H$ (Table 3). Differences between mean values of $\delta^{18}O$ are significant for snow and the three ice types. There is no significant difference between values of $\delta^{2}H$ in firn ice and congelation ice, but melt ice and snow are significantly different.

Further insight is provided by investigating the relationship between $\delta^{18}O$ and $\delta^{2}H$ in the different types of ice. Plotting the five samples from the snow cone in $\delta^{18}O$ and $\delta^{2}H$ space yields a slope of 8.3 and an intercept of 4.6‰. This result is similar to the local meteoric water line (slope 8.0 and intercept of 8.1‰) developed from 68 snowpack and precipitation samples collected in the surrounding region between 1999 and 2001 (Benjamin et al., 2005). Furthermore, plotting the five snow cone samples along with the 29 samples of firn ice from exposures A and B yields a slope of 8.0 and an intercept of –1.4‰ (Fig. 8), which is nearly identical to the slope of 7.4 and intercept of –2‰ for a winter local meteoric water line derived from 46 snow samples in that same study (Benjamin et al., 2005), supporting the interpretation that the firn ice is formed directly through densification of snow. In contrast, the 11 samples of melt ice collected from the base of exposure B, and from a single layer in Strickler's Throat (exposure C), yield a slope of 6.1 with a very low intercept of –30.4‰ (Fig. 8). Slopes of that magnitude are evidence of melting and refreezing of ice in subglacial settings, and a similar mechanism is likely responsible here (Jouzel and Souchez, 1982). Between these two extremes, the 34 samples of congelation ice collected from exposure D yield a slope of 7.0 and an intercept of –17.3‰ (Fig. 8). This low intercept indicates that these samples were impacted by kinetic effects during refreezing, but this slope is still close to the local meteoric water line, suggesting that these effects have not completely overprinted the original isotopic signal.

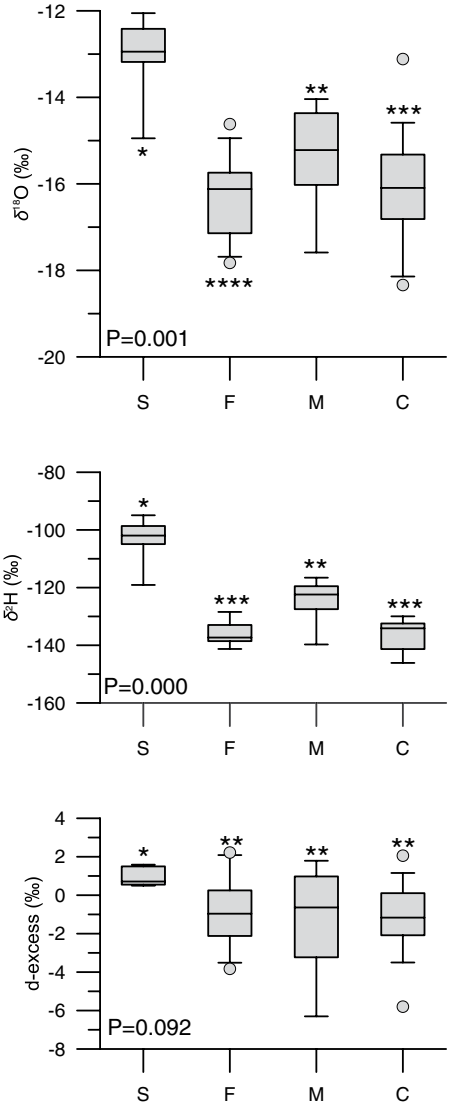


**Figure 7. Box plots presenting water stable isotope characteristics grouped by ice type: S—snow, F—firn, M—melt, C—congelation. Horizontal lines mark the median, boxes span the interquartile range, whiskers define the 5/95 percentile range, and outliers are shown as gray circles. Stars identify groups that are statistically distinct with a Mann-Whitney test. *P* values in lower left reflect the significance of differences between all four groups assessed with a Kruskal-Wallis test.**

When plotted in $\delta^{18}O$ and $\delta^{2}H$ space, all samples are shifted down and to the right from the local meteoric water line (Fig. 8). This shift indicates enrichment in heavier isotopes (Lechler and Niemi, 2011), which is signaled by the notably low intercepts for lines fit to the Strickler

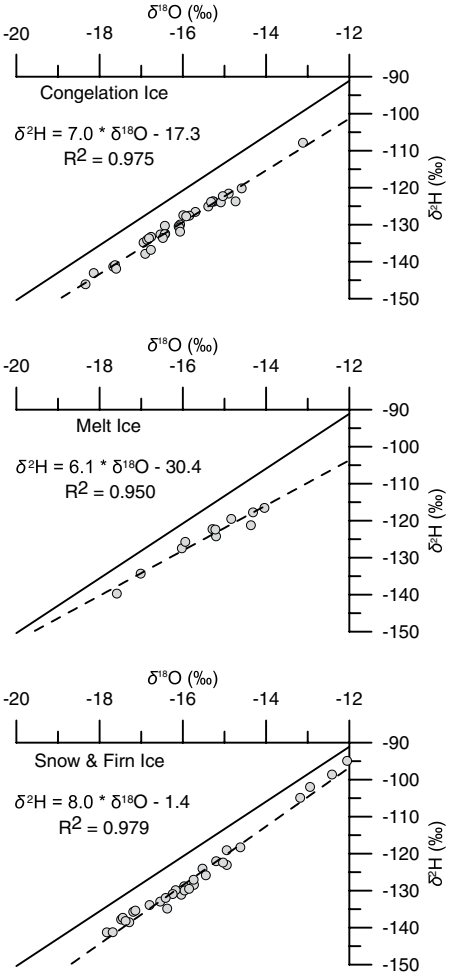


**Figure 8. Stable isotope results for three types of ice presented in $\delta^{18}O$ and $\delta^{2}H$ space. Solid sloping line is the local winter meteoric water line ($y = 7.41x - 2.41$) from Benjamin et al. (2005).**

Cavern data (Fig. 8). The standard global meteoric water line has an intercept of 10‰ (Craig, 1961). In contrast, lines fit to the samples representing different types of ice in Strickler Cavern have intercepts ranging from 5‰ (snow) to as low as –30‰ (melt ice). This situation is further highlighted by calculation of deuterium excess (d-excess), a metric used to quantify departure from the global meteoric water line, which has a d-excess of 10‰ (Dansgaard, 1964; Froehlich et al., 2001). All the samples from Strickler Cavern have d-excess values <10‰, including some negative values (Table 3; Fig. 7). Low intercepts and d-excess values <10‰ can reflect aspects of the local precipitation (Froehlich et al., 2001), and this explanation appears valid for Strickler Cavern. As noted previously, the winter local meteoric water line for the region surrounding the cave has an intercept of –2‰ (Benjamin et al., 2005), similar to the –1.4‰ for the snow and firn ice samples ($n = 34$) in this study (Fig. 8). Similarly, a regression fit to monthly values of $\delta^{18}O$ and $\delta^{2}H$ estimated for the cave location through spatial interpolation (Bowen and Revenaugh, 2003; Bowen and Wilkinson, 2002) also has a low intercept (–4.3‰). Furthermore, values of d-excess generally <5‰ have been reported for cave ice in the Canadian Rockies, and interpreted as a consequence of a drier, more evaporative climate inland from the coast (Yonge, 2014; Yonge and MacDonald, 1999). Thus, low intercept and d-excess values are characteristic of snow in the interior parts of the northern Rocky Mountains, and this property carries over to the snow and firn ice in the cave.

As shown in Table 3, mean d-excess is even lower for the congelation ice (–1.2‰) compared with the firn ice (–0.8‰). Although this difference is not statistically significant ($P = 0.166$), the lower mean and minimum values suggest that some process is depressing d-excess in the congelation ice beyond the already low values characteristic of winter precipitation in this area. Previous studies have documented enrichment of heavy isotopes in snow by sublimation (Lechler and Niemi, 2011). Although there has been debate over whether this process impacts the entire snowpack or just the surface layers (Moser and Stichler, 1974; Stichler et al., 2001), Lechler and Niemi (2011) concluded that sublimation during the winter can have a significant impact on snowpack stable isotope composition. This impact is particularly pronounced in the orographic precipitation shadow along the eastern side of the Sierra Nevada, where snow persists for many months under dry climatic conditions (Lechler and Niemi, 2011). Similar conditions prevail in the Lost River Range, making it likely that snowpack in the vicinity of Strickler Cavern is progressively affected by sublimation over the course of the winter, enriching heavy isotopes and decreasing d-excess values. When the snowpack melts, this sublimation-influenced water soaks into the ground, descends to the cave, and freezes as in addition to the stalagmite. The signature of this sublimation influence is retained in the congelation ice in the form of low intercept and d-excess values. In contrast, snow that falls into the cave entrance would be less influenced by sublimation due to humid conditions in the cave and lack of exposure to the sun, explaining the generally higher d-excess values in the firn ice (Table 3).

### *Stable Isotopes Summary*

Measurement of stable isotopes supports the interpretation that three main types of ice are present in Strickler Cavern. Firn ice and congelation ice samples exhibit slopes in $\delta^{18}O$ and $\delta^{2}H$ space that are similar to the winter local meteoric water line. In contrast, samples of melt ice have a much lower slope, indicative of fractionation during melting and refreezing. Values of intercept and d-excess in snow and firn samples are low, but they are similar to those reported from previous studies of snow and cave ice in the northern Rocky Mountains. Even lower values in congelation ice likely reflect the impact of snowpack sublimation at the surface during the winter, an effect that is inconsequential in the humid, dark conditions of the cave. Fractionation during melting and refreezing complicates interpretation of the melt ice samples. However, samples of firn and congelation ice likely retain an interpretable isotope signal of winter precipitation.

### *Paleoenvironmental Implications*

Previous studies have concluded that static ice caves, like Strickler Cavern, are sensitive recorders of winter precipitation and are relatively unaffected by summer conditions (Luetscher et al., 2005). Because large volumes of air are only able to enter the cave through density settling, mixing is dramatically reduced when the outside air temperature rises above the ambient cave temperature (Luetscher and Jeannin, 2004). As a result, the cave atmosphere preferentially samples the colder part of the year, promoting maintenance of freezing conditions year-round. Shifts toward warmer or cooler summer conditions at the surface would do little, if anything, to alter this situation. Furthermore, given the strong seasonality of precipitation in this area, with 64% of the annual moisture arriving during months with average temperature <0 °C (November–April), precipitation arriving as snow is likely to dominate the signal recorded in the cave. As a result, it is reasonable to consider the ice in Strickler Cavern to be a record of past winter precipitation (Stoffel et al., 2009).

In this interpretive framework, it is notable that firn ice samples from exposures A and B have considerably lower mean isotope values (mean $\delta^{18}O$ of –16.3‰) than those from the near-modern samples from the snow cone and the top of the stalagmite (mean $\delta^{18}O$ of –14.3‰). Because stable isotopes in precipitation are strongly influenced by air temperature (Dansgaard, 1964), this difference, which is highly significant ($P = 0.000$), indicates that the older samples were deposited during colder winters. The Bayesian analysis suggests that the ice comprising exposures A and B accumulated during the early part of the Little Ice Age, between the late 1600s and mid-1700s. Using the linear relationship ($r^2 = 0.820$) between

average air temperature for months with subzero mean temperatures and mean $\delta^{18}O$ estimated for the Mill Creek Summit SNOTEL site with the Online Isotopes in Precipitation Calculator (http://wateriso.utah.edu/waterisotopes/index.html), an ~2‰ difference in $\delta^{18}O$ equates to a temperature change of ~2.4 °C, providing a rough estimate for winter temperature depression at Strickler Cavern during the Little Ice Age. For comparison, $\delta^{18}O$ values measured in an ice core from Upper Fremont Glacier in the Wind River Range, ~400 km to the southeast of Strickler Cavern, combined with site-specific transfer functions for $\delta^{18}O$ and air temperature, suggest that conditions during the latter part of Little Ice Age (ca. A.D. 1740–1860) were ~5 °C cooler than modern (Naftz et al., 2002). Greater cooling at Upper Fremont Glacier may be a function of the higher elevation of the glacier coring site (4000 m vs. 2500 m) if climatic changes during the Little Ice Age impacted higher elevations disproportionately. Alternatively, the difference may reflect a seasonal bias, given that Strickler Cavern primarily samples the winter months, whereas the precipitation data used to derive the transfer functions linking temperature and $\delta^{18}O$ for the Upper Fremont Glacier were annual (Naftz et al., 2002). It is also possible, due to limited accessibility, that the sampling strategy in Strickler Cavern simply failed to collect ice that accumulated as snow during the coldest part of the Little Ice Age, leaving the true $\delta^{18}O$ minimum in the Strickler Cavern ice unknown.

Notable trends are also apparent in the $\delta^{18}O$ values measured for contiguous samples. For instance, the longest series of samples ($n$ = 15) from conformable layers of firn ice was collected from exposure B (Fig. 3). Values of $\delta^{18}O$ start out relatively high (~–15.0‰) at the base of this exposure and drop steadily, reaching a minimum of –16.8‰ near the top (Fig. 9). Results of the Bayesian analysis, corroborated by visual layer counting, reveal that this sequence accumulated over ~30 yr (ca. A.D. 1700–1730). Thus, the accessible ice within exposure B may record part of the cooling toward peak Little Ice Age conditions in the early eighteenth century.

Plotting all of the congelation ice, firn ice, and modern snow samples in chronological order further highlights the uniqueness of the most recent precipitation (Fig. 9). This approach also reveals that the decreasing values of $\delta^{18}O$ leading into the Little Ice Age maximum are superimposed on an overall trend of rising $\delta^{18}O$. It is important to note that the available age control precludes quantification of the absolute ages of these samples; particularly in the case of the stalagmite, numerous unconformities mark places where unknown amounts of ice and time are missing from the record. As noted earlier, kinetic effects during refreezing may also have impacted the congelation ice samples. Nonetheless, the rising trend in $\delta^{18}O$ is clear, but its significance is difficult to determine. Many of the samples comprising this trend were collected from the stalagmite. The oldest samples, with the most negative $\delta^{18}O$ values, generally have the highest d-excess values, and d-excess decreases upward through the stalagmite. Because lower d-excess values correspond to greater degrees of sublimation, this trend may reflect a shift toward a more sublimation-influenced snowpack over time.

Overall, given the available age control, it is clear that ice in Strickler Cavern records winter precipitation that accumulated during the Little Ice Age. Further analysis of stable isotopes in this ice could yield more refined quantitative estimates of Little Ice Age climatic conditions in the northern Rocky Mountains, particularly when combined with tree-ring records (e.g. Naftz and Smith, 1993) and high-resolution lacustrine records (e.g. Munroe et al., 2012, 2013). Furthermore, on the basis of results from the Upper Fremont Glacier core, the Little Ice Age in the Wind River Range apparently ended abruptly in ~10 yr around A.D. 1845 (Schuster et al., 2000). The radiocarbon ages in this study span this interval; therefore, it is reasonable to assume that the ice within Strickler Cavern also contains a record of how the Little Ice Age ended, possibly permitting the duration of this transition to be quantified and its abruptness and synchronicity to be assessed.

## Glaciochemistry

### *Detectable Elements*

Analysis of 78 melted ice samples with ICP-MS identified 14 elements that were consistently above detection limits in all samples (Table 4). By far the most abundant element was Ca, with an average concentration of ~18,000 ppb (Fig. 10). Abundances of Na, Mg, and K were similar, around 4000 ppb. Other major elements, including Fe (89 ppb), Al (48 ppb), and Mn (10 ppb), were also detectable. The most abundant trace elements were Ba (56 ppb) and Sr (45 ppb). Abundances of Ni, Ti, Zn, As, and Rb averaged <40 ppb. Many elements exhibited strong correlations; for instance, Ca was significantly (positively) correlated with Mg, K, Ti, Fe, As, Rb, Sr, and Ba. Calcium also had a significant negative correlation with Zn. Similarly, Na, the second most abundant element, was significantly (positively) correlated with Mg, K, Ni, and Rb. The strongest positive correlations were between Ca and Ti (0.998), Fe and Ti (0.945), Ca and Sr (0.941), Ti and Sr (0.936), and between K and Rb (0.917).

Grouping the glaciochemistry results by ice type reveals some notable similarities and differences. For instance, abundances of Ca and Fe were highest in the firn and congelation ice and were much lower in snow and melt ice (Fig. 11). In contrast, Al and K followed the opposite trend, with highest values in the melt ice and the lowest values in the congelation ice. Sodium, Ni, Zn, and Rb reached maximum values in the snow; Zn was particularly enriched, with average values ~8× higher than in other ice types.

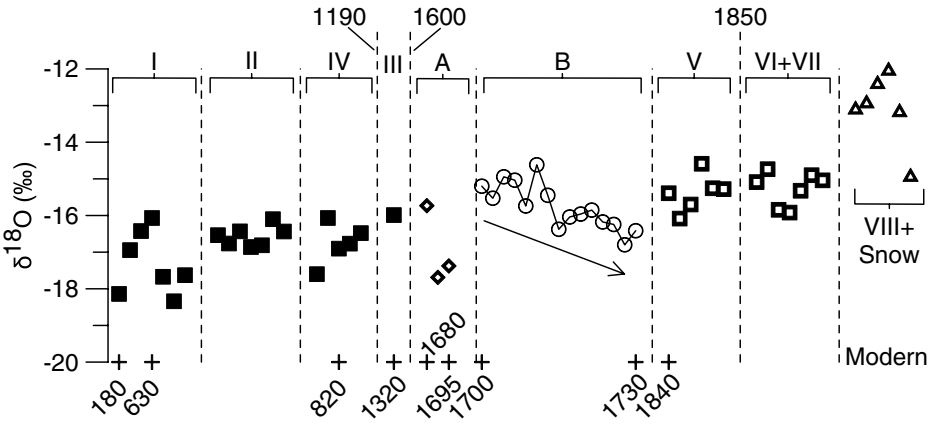


**Figure 9. $\delta^{18}O$ results from congelation ice (squares) and firn ice and snow (other symbols) arranged in stratigraphic order. Crosses mark calibrated radiocarbon ages in years A.D. Vertical dashed lines denote unconformities. Brackets at top designate concordant packages of layers in the stalagmite (roman numbers, Fig. 5) and firn ice (exposures A and B). Arrow highlights the decreasing $\delta^{18}O$ values in contiguous samples from exposure B. Modern samples from unit VIII and the snow cone are clearly different than the older samples. Kinetic effects during freezing may have impacted the congelation ice, but long-term trends are still notable.**

TABLE 4. BASIC STATISTICS SUMMARIZING GLACIOCHEMISTRY RESULTS FOR ICE SAMPLES FROM STRICKLER CAVERN

| Ice type | Statistic | Ca (ppb) | K (ppb) | Na (ppb) | Mg (ppb) | Fe (ppb) | Ba (ppb) | Al (ppb) | Sr (ppb) | Ni (ppb) | Ti (ppb) | Zn (ppb) | Mn (ppb) | As (ppb) | Rb (ppb) | PC-1 | PC-2 | PC-3 |
|---|---|---|---|---|---|---|---|---|---|---|---|---|---|---|---|---|---|---|
| All | Mean | 18,374 | 4401 | 4179 | 3966 | 88.8 | 56.2 | 48.1 | 44.7 | 38.6 | 27.9 | 12.6 | 9.9 | 6.0 | 1.6 | 0.00 | 0.00 | 0.00 |
| *n* = 79 | Median | 15,398 | 1688 | 2963 | 1895 | 75.8 | 45.5 | 36.2 | 35.8 | 27.3 | 23.3 | 4.8 | 3.2 | 2.6 | 0.8 | –0.20 | –0.28 | 0.09 |
| | St dev | 11,308 | 6766 | 3274 | 4480 | 55.4 | 39.5 | 35.8 | 33.1 | 54.5 | 17.0 | 34.4 | 17.4 | 8.4 | 2.3 | 1.00 | 1.00 | 1.00 |
| | Max | 49,468 | 39,634 | 24,440 | 23,645 | 264.7 | 183.3 | 218.2 | 176.1 | 461.2 | 74.3 | 294.5 | 107.7 | 47.5 | 15.7 | 3.10 | 6.70 | 4.08 |
| | Min | 1094 | 129 | 1245 | 326 | 8.2 | 1.9 | 2.3 | 2.3 | 0.6 | 1.8 | 1.3 | 0.1 | 0.3 | 0.2 | –1.34 | –0.82 | –3.54 |
| Snow | Mean | 8735 | 4520 | 8067 | 822 | 48.6 | 44.9 | 39.2 | 14.6 | 119.2 | 13.4 | 84.3 | 11.5 | 1.1 | 5.2 | –0.95 | 1.63 | 0.96 |
| *n* = 5 | Median | 6426 | 2442 | 5184 | 617 | 34.6 | 22.1 | 27.9 | 8.8 | 3.8 | 9.5 | 22.7 | 3.6 | 1.0 | 2.4 | –1.17 | 0.46 | 0.25 |
| | St dev | 6117 | 5706 | 9249 | 689 | 31.7 | 38.6 | 28.6 | 12.0 | 198.8 | 9.6 | 119.9 | 19.2 | 0.8 | 6.0 | 0.50 | 2.84 | 1.78 |
| | Max | 18,933 | 14,637 | 24,440 | 1995 | 102.0 | 101.9 | 79.7 | 35.0 | 461.2 | 29.4 | 294.5 | 45.7 | 2.2 | 15.7 | –0.09 | 6.70 | 4.08 |
| | Min | 4209 | 1054 | 2138 | 326 | 22.8 | 12.3 | 14.3 | 5.5 | 0.6 | 6.4 | 10.5 | 0.3 | 0.3 | 1.4 | –1.34 | 0.10 | –0.25 |
| Firn ice | Mean | 20,694 | 4547 | 4294 | 4943 | 108.6 | 39.7 | 58.2 | 45.1 | 37.9 | 31.3 | 10.5 | 16.5 | 5.1 | 1.2 | 0.11 | 0.00 | –0.34 |
| *n* = 28 | Median | 16,585 | 2359 | 4140 | 3803 | 97.4 | 32.0 | 49.7 | 34.2 | 33.5 | 26.0 | 6.8 | 7.6 | 2.9 | 0.9 | –0.13 | –0.05 | –0.15 |
| | St dev | 12,814 | 4871 | 2210 | 4238 | 68.3 | 32.6 | 39.3 | 30.3 | 17.3 | 19.2 | 10.6 | 24.6 | 5.4 | 0.7 | 1.04 | 0.43 | 1.00 |
| | Max | 49,468 | 19,340 | 10,213 | 13,402 | 264.7 | 134.5 | 218.2 | 113.5 | 89.6 | 74.3 | 43.2 | 107.7 | 22.1 | 3.1 | 2.69 | 1.06 | 1.55 |
| | Min | 3757 | 594 | 1529 | 566 | 23.6 | 6.2 | 24.5 | 8.2 | 16.8 | 5.8 | 1.5 | 0.3 | 0.5 | 0.4 | –1.17 | –0.60 | –3.54 |
| Melt ice | Mean | 14,828 | 6731 | 4792 | 5781 | 68.9 | 35.1 | 57.8 | 33.9 | 45.0 | 22.3 | 10.2 | 7.7 | 3.2 | 1.8 | –0.24 | 0.20 | –0.34 |
| *n* = 10 | Median | 7602 | 3887 | 4430 | 4666 | 45.6 | 27.7 | 48.6 | 17.6 | 36.5 | 11.6 | 7.0 | 2.5 | 2.2 | 1.4 | –0.67 | 0.07 | –0.39 |
| | St dev | 13,738 | 6399 | 2289 | 4441 | 61.8 | 35.6 | 28.6 | 33.6 | 41.9 | 20.6 | 13.6 | 11.2 | 4.4 | 1.4 | 1.07 | 0.62 | 0.82 |
| | Max | 43,746 | 18,844 | 9081 | 12,544 | 215.7 | 122.2 | 117.4 | 99.9 | 159.8 | 66.0 | 46.7 | 36.6 | 15.4 | 4.8 | 2.17 | 1.19 | 1.20 |
| | Min | 1094 | 333 | 1711 | 1112 | 8.2 | 1.9 | 8.4 | 2.3 | 11.3 | 1.8 | 1.3 | 1.0 | 0.5 | 0.4 | –1.31 | –0.82 | –1.83 |
| Congelation ice | Mean | 18,907 | 3602 | 3357 | 3116 | 84.3 | 77.1 | 38.6 | 51.8 | 25.8 | 28.8 | 4.7 | 5.1 | 8.3 | 1.3 | 0.12 | –0.29 | 0.23 |
| *n* = 35 | Median | 15,477 | 800 | 2473 | 1443 | 74.4 | 67.1 | 30.5 | 41.1 | 20.7 | 23.6 | 3.7 | 1.6 | 3.2 | 0.5 | –0.15 | –0.53 | 0.30 |
| | St dev | 9096 | 8240 | 2431 | 4686 | 37.8 | 36.8 | 33.9 | 35.0 | 15.5 | 13.7 | 4.9 | 8.2 | 10.9 | 2.2 | 0.95 | 0.76 | 0.77 |
| | Max | 43,278 | 39,634 | 13,681 | 23,645 | 195.0 | 183.3 | 160.0 | 176.1 | 76.5 | 66.2 | 31.8 | 43.3 | 47.5 | 11.2 | 3.10 | 2.91 | 2.08 |
| | Min | 8876 | 129 | 1245 | 336 | 44.3 | 22.7 | 2.3 | 13.3 | 7.3 | 13.8 | 2.0 | 0.1 | 1.2 | 0.2 | –0.66 | –0.71 | –2.30 |

*Note*: Max—maximum; Min—minimum; St dev—standard deviation; PC-1, -2, -3—principal component 1, 2, and 3, respectively.

Ca, Fe, Al, Ti, and Mn were most abundant, on average, in the firn ice, whereas K and Mg were most abundant in the melt ice. Only Ba, Sr, and As were most abundant in the congelation ice; Ba was particularly abundant in this ice type. Differences in the average values of each of the 14 detectable elements were significant ($P < 0.050$) using a Kruskal-Wallis test. Differences for Zn, Rb, and Ba were most significant ($P = 0.000$), whereas differences for Ca and Ti were marginal ($P = 0.045$).

### *Principal Component Analysis*

Principal component analysis (PCA) was employed to simplify the overall glaciochemistry data set, revealing major trends and correlations. Results of a Kaiser-Meyer-Olkin measure of sampling adequacy (0.747) and Bartlett's test of sphericity ($P = 0.000$) demonstrate the suitability of the data set for PCA. The rotation converged in six iterations, and the resulting first three principal components (PC) had eigenvalues >1.0 and collectively explain 72% of the variance (Fig. 12). Maximum communalities (>0.800) were obtained for Ca, Ti, Sr, Na, K, Fe, and Rb. The lowest communalities were for Mn (0.305), Ni (0.326), and Ba (0.375). Consideration of the pattern matrix resulting from the PCA reveals that Ti (0.964), Ca, Sr, Fe, Mg, As, K, and Ba (0.527) load onto PC-1, with scores in descending order (Fig. 12). PC-2 is dominated by Rb (0.891), Na, Zn, K, and Mn (0.448), in descending order. Only Ni (0.552) loads positively onto PC-3, although Al exhibits a strong negative relationship (–0.810) with PC-3.

Consideration of these principal components by ice type reveals that scores for PC-1 are lowest in the snow samples and highest in the firn ice (Fig. 11; Table 4). In contrast, PC-2 is highest in the snow and lowest in the congelation ice. The overall maximum value (6.7) was obtained for a sample from the 2013–2014 layer in the snow cone that had unusually high abundances of Na, Rb, Mn, and Zn. Snow samples also had the highest average values for PC-3, driven in part by a Ni content of 461 ppb in the deepest sample from the snow cone. Differences between mean values of the three principal components were significant ($P < 0.050$) using a Kruskal-Wallis test.

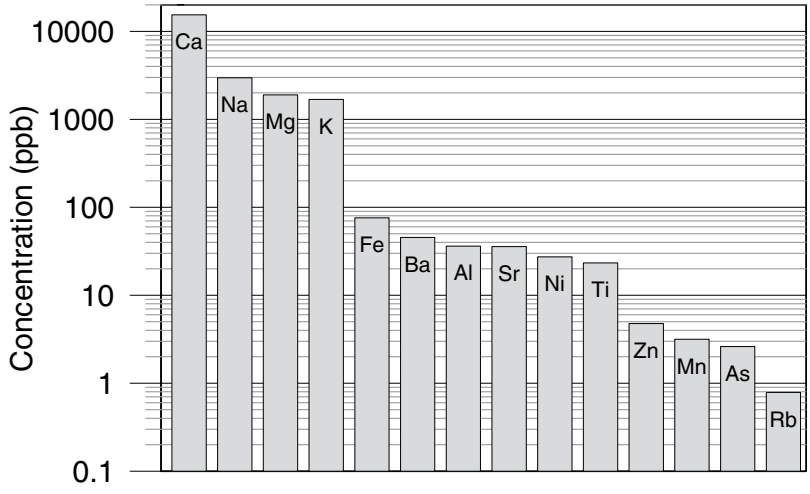


**Figure 10. Median concentrations of detectable elements in ice from Strickler Cavern. Elemental abundances are in ppb.**

### *Glaciochemistry Interpretation*

Little work has been published on the glaciochemistry of cave ice. The most comprehensive study focused on Vukušic Cave in Croatia (Kern et al., 2011b), which contains an accumulation of firn and congelation ice up to 15 m thick and lacks dynamic ventilation, making it similar to Strickler Cavern. Two cores were collected from this ice, and abundances of 45 different elements were measured with ICP-MS. In total, 36 samples was analyzed, and 23 elements were above the detection limit at least one sample; 12 elements were detected in all 36 samples (Kern et al., 2011b). As in Strickler Cavern, Ca was the most abundant element, with a median abundance of 3660 ppb and a maximum of

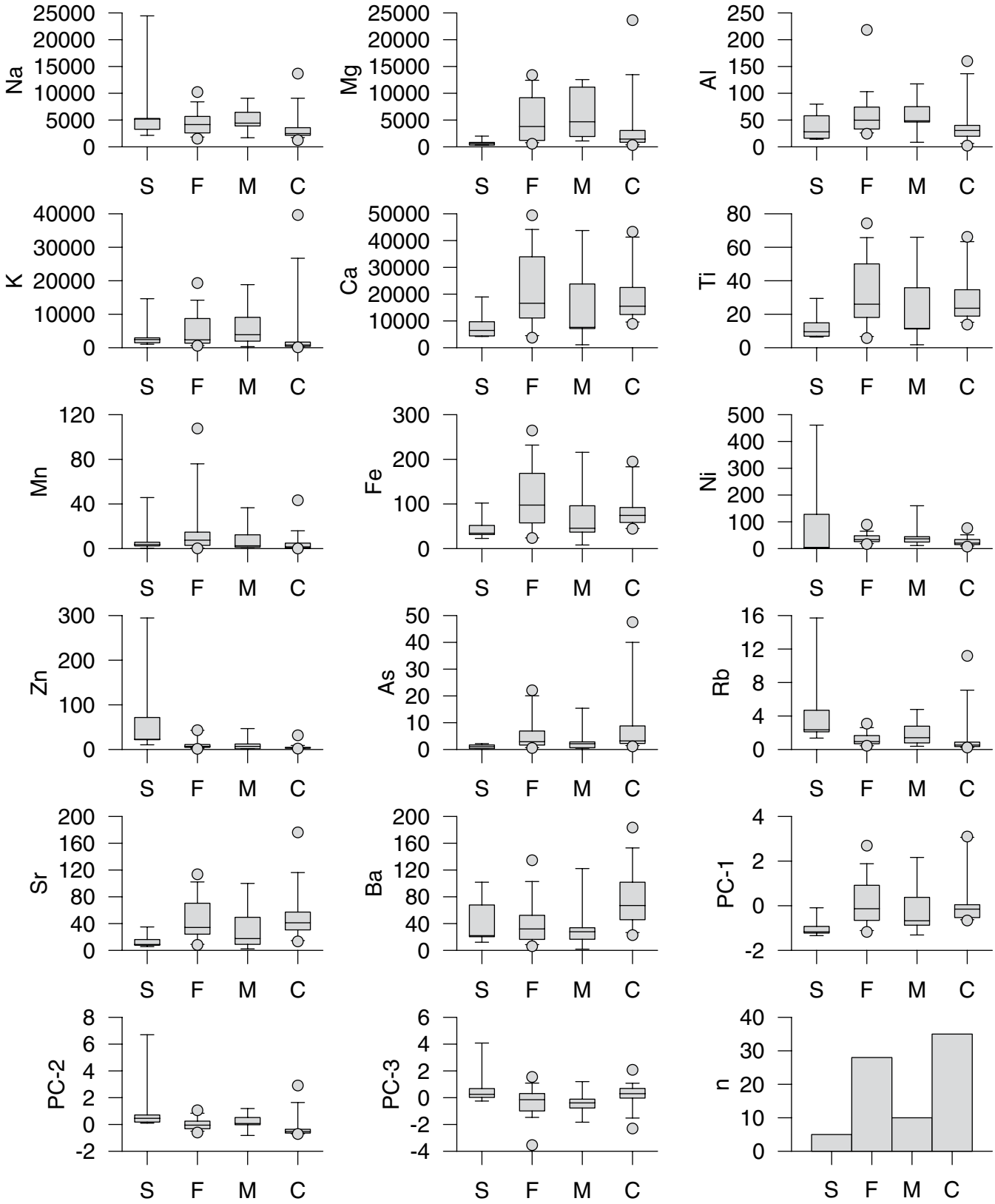


**Figure 11. Box plots presenting glaciochemistry results grouped by ice type: S—snow, F—firn, M—melt, C—congelation. Horizontal lines mark the median, boxes span the interquartile range, whiskers define the 5/95 percentile range, and outliers are shown as gray circles. Elemental abundances are in ppb. Values for the first three principal components (PC) are also shown, along with the number of each sample type (*n*).**

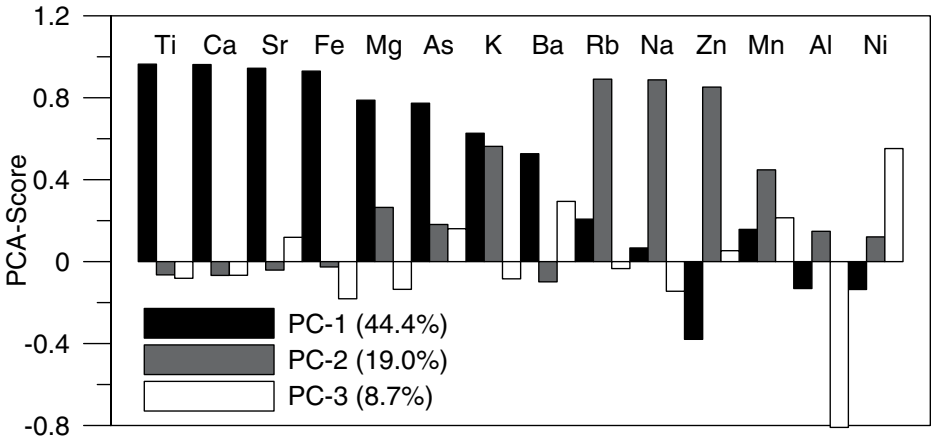


**Figure 12. Results of principal component analysis of ice from Strickler Cavern. The first three components have eigenvalues >1.0 and collectively explain 72% of the variance. Ti, Ca, Sr, Fe, Mg, As, K, and Ba load on PC-1. Ru, Na, Zn, Mn, and Al load on PC-2. PC-3 is governed by Ni.**

47,500 ppb. Na and Mg were present at median abundances >60 ppb. Al, Zn, Fe, Mn, and Sr were considered minor components, with median concentrations between 3 and 50 ppb. Trace components, including Cr, As, Rb, Pb, K, Co, Cu, Ce, and U, were detectable in most samples, but in some cases, they were below the limit of detection.

Ten of the 12 elements above the detection limit in all samples from Vukušic Cave were also detectable in Strickler Cavern; the exceptions were Cr and Pb. In contrast, Ba, Ni, and Ti were present at median abundances from 20 to 45 ppb in Strickler Cavern but were below the detection limit in Vukušic Cave. Seven elements were more abundant in Strickler Cavern. Enrichment was greatest for Mg (30×), As (13×), Sr (12×), and Na (12×). Three elements were more abundant in Vukušic: Zn (7×), Mn (2×), and Al (1.4×). K was 8× more abundant in Strickler Cavern (median of 1688 ppb vs. 210 ppb), but because it was below the detection limit in some of the Vukušic samples, it was excluded from further analysis (Kern et al., 2011b).

Elevated abundances of Ca and Mg are reasonable for both caves, given that they formed in carbonate bedrock, and the greater abundance of Mg in the Strickler Cavern ice likely reflects hosting of the cave in dolomite. Calcium is also the most abundant element measured in snow from two snowpack chemistry monitoring sites (Galena Summit and Banner Summit) at similar elevations <100 km west of Strickler Cavern (https://co.water.usgs.gov/projects/RM_snowpack/). Abundances of Ca and Mg were positively correlated in these snow samples, as they were in the samples from the snow cone ($r^2$ = 0.993). Abundances of K and Na are also routinely measured at the snowpack monitoring sites. Na tends to be more abundant than K, and the same relationship is seen in the ice and snow from Strickler Cavern (Table 4). Thus, there is general consistency between the four most abundant elements in the ice of Strickler Cavern and measurements made at nearby snowpack monitoring sites.

Kern et al. (2011b) conducted a PCA of the glaciochemistry results from Vukušic Cave, identifying three principal components with eigenvalues in excess of 1.0. The first principal component was dominated by Ca, Mg, Mn, As, Rb, and Sr. Na, Cr, and Pb loaded onto the second principal component. Because K covaries with many of these elements, it was thought to fit here as well. Finally, PC-3 was controlled by Al and Fe. In a comparison with the results from Strickler Cavern, Ca, Mg, As, and Sr are found on PC-1 in both data sets, whereas Na is common to PC-2. Fe, which was found on PC-3 in Vukušic Cave was grouped with PC-1 in Strickler Cavern. Al was also part of PC-3 in Vukušic Cave, but it exhibited a strong inverse relationship with PC-3 in the Strickler Cavern data set. Finally, Ni dominated PC-3 in Strickler Cavern but was not detected in Vukušic Cave.

Kern et al. (2011b) interpreted PC-1 as a sign of local bedrock influence, given the presence of these elements in the rocks surrounding the cave. The same logic is reasonable for Strickler Cavern; however, because much of the ice in Strickler is derived from snow rather than seepage water, these elements must be delivered as regional dust that becomes entrained in the precipitation. Alternatively, these elements could become incorporated as fine particles detach from the walls of the cave, are buried in the snow, and slowly dissolved. The presence of Fe and Ti on PC-1 in Strickler Cavern may reflect the presence of mafic volcanic rocks in the vicinity that could act as local sources of iron. Ba, which was most abundant in the congelation ice, is also strongly correlated with PC-1 in Strickler Cavern. Thus, a source of Ba in the soil or epikarst must be dissolved by water that penetrates the ground in transit to the cave.

The elements comprising the second principal component in Vukušic Cave were interpreted as a signal of atmospheric transport. Metals such as Cr and Cu were considered to reflect mining activity, Pb from the combustion of leaded gasoline, and Na and K as aerosols transported from the Mediterranean Sea (Kern et al., 2011b). Atmospheric transport as mineral dust is also a reasonable interpretation for the elements on PC-2 in Strickler Cavern. Atmospheric deposition of dust containing feldspars could explain the Na, K, and Rb, whereas Zn could reflect the presence of sulfide mining operations in the Rocky Mountain region.

The third principal component in Vukušic Cave (Al and Fe) was considered a signal of mineral dust deposition. In the Strickler Cavern data set, Fe was associated with PC-1, and Al exhibited a very strong negative relationship with PC-3. Only Ni had a strong positive correlation with PC-3, suggesting atmospheric transport from another regional mining source. It is notable, however, that the two most obvious mining-related elements (Zn and Ni) load strongly onto separate components, implying that they are coming from different sources, perhaps transported by divergent wind directions. The fact that both Ni and Zn are greatly elevated in the samples from the snow cone is supports the theory that they signify recent, anthropogenic components of the mineral dust flux in this region. As corroboration, it is notable that work ~500 km to the southeast of Strickler Cavern has documented enrichment of Ni, Zn, and other mining-related metals in modern dust (Reynolds et al., 2013; Munroe, 2014; Munroe et al., 2015).

It is also illuminating to consider trends in elemental abundances through selections of samples with known stratigraphic relationships. Several elements exhibited dramatically elevated abundances in samples from sections II and IV in the stalagmite (Fig. 5), which was not directly dated but accumulated sometime after A.D. 630 and before A.D. 1190. These include Na, Mg, K, Ca, Ti, Mn, Fe, Ni, As, Rb, and Sr. In contrast, Al and Zn were not elevated appreciably in these layers; Zn, notably, was fairly consistent in abundance until the top of the stalagmite. The significance of this pattern is unclear, but it suggests that the chemistry of

water reaching the stalagmite changed. Elements associated with all three of the principal components rise in units II and IV, and both PC-1 and PC-2 are high in this interval as well. However, ratios of elements sharing an affinity to a specific principal component, for instance, Ca/Ti and Fe/Ti, remained essentially constant through the interval of elevated abundances, whereas ratios that combined components, for instance, Ca/Rb, Sr/Rb, and Na/K, dropped considerably. This divergence suggests an increase in the abundance of elements arriving as dust (primarily PC-2) in relation to those reaching the cave through snowfall (primarily PC-1). Collection and analysis of larger ice samples could permit detection of additional trace elements that could be useful as fingerprints of eolian dust deposition.

## DIRECTIONS FOR FUTURE WORK

The results of this study provide a solid foundation upon which additional investigations of the ice in Strickler Cavern could be based. One of the most obvious directions is to extract a continuous core through the firn ice deposit (e.g. Kern et al., 2011a; May et al., 2011). Because the internal stratigraphy of the ice is unknown, and its total thickness is not constrained by the available exposures, ground penetrating radar (Behm and Hausmann, 2007; Hausmann and Behm, 2010) or another geophysical technique could be employed to identify the optimum site in which to drill. Analysis of samples collected from individual layers in the snow cone over consecutive years could reveal changes in stable isotope ratios during snow densification. Repeat monitoring of the dimensions of the ice deposit could also be useful for documenting effects of climate change (Luetscher et al., 2005; Kern and Perşoiu, 2013; Colucci et al., 2016). Further study could also focus on the organic matter contained within the ice. For instance, analysis of macrofossils could reveal changes in the composition of the forest surrounding the cave entrance over time (Reasoner and Jodry, 2000). Similarly, study of pollen, which is likely preserved within the ice (e.g., Feurdean et al., 2011), could reveal information about vegetation changes in the broader region surrounding the cave. Analysis of microcharcoal could provide information about changes in forest fire regimes over time (Power et al., 2008). Filtering and analysis of insoluble particulates from the ice could shed light on changes in eolian dust deposition in this part of the Rocky Mountains (Vandenberghe, 2013; Munroe et al., 2015). Particulate analysis, perhaps combined with electrical conductivity measurements on an ice core, could also provide a useful cryptotephra record (Abbott and Davies, 2012) that would refine age estimates for the ice, as was done for the core from the Upper Fremont Glacier in Wyoming (Schuster et al., 2000). Study of sulfate, nitrate, and Hg abundance in the ice could clarify preindustrial values for these anthropogenically influenced pollutants. Analysis of short-lived radionuclides such as tritium and cesium could help assign ages to the youngest part of the ice deposit (Kern et al., 2009; Kern et al., 2011a). This approach could also be valuable in developing an age model for parts of the stalagmite that are devoid of organic matter. Finally, the uranium content of the congelation ice may be elevated enough to permit U-series dating (Cheng et al., 2013) of the ice itself. This approach, if successful, would provide a new avenue for assigning absolute ages to cave ice that could have broad applicability beyond Strickler Cavern.

## CONCLUSION

This project involved a comprehensive investigation of the chronology, stable isotopes, and glaciochemistry of a significant and previously unstudied cave ice deposit in Idaho, United States. Strickler Cavern, in the Lost River Range of Idaho, contains an accumulation of stratified ice nearly 30 m thick that formed through densification of snow that accumulates within the vertical entrance shaft each winter. Cold air enters the cave in winter through density settling, but buoyant warmer air is unable to penetrate the cave in summer. As a result, cave temperatures remain below freezing year-round, and perennial ice is preserved. Water dripping from the ceiling also freezes in the cave, forming stalagmites of congelation ice. Local melting of the ice in the cave entrance produces a shallow pond of water that forms melt ice when it refreezes. Melt ice is also produced when meltwater from higher parts of the cave descends to lower, colder levels.

In total, 26 radiocarbon dates on organic matter incorporated within the ice provided age control. On the basis of these results, the congelation ice forming the stalagmite accumulated over the past 2000 yr, with numerous unconformities representing episodes of melting. A major melting event near the end of the Little Ice Age resulted in the loss of much ice that accumulated between A.D. 1200 and 1850. Melting may have been driven by changes in the thermal balance of the cave system induced by plugging of the entrance shaft with snow. Ice accumulation resumed after this melting episode and remains an ongoing process.

The stratified ice deposit is younger, having accumulated over the past four centuries. Given the stratigraphic relationships between the organic samples from this deposit, a Bayesian statistical analysis was applied to refine the calibrated radiocarbon age estimates. This approach suggests an overall ice accumulation rate of ~9 cm/yr, which is consistent with the observed thickness of ice layers between concentrations of organic matter.

Stable isotopes within the ice may have been modified by postdepositional effects, but stratigraphic trends in stable isotopes likely still contain an interpretable paleoclimate signal. Stable isotopes are heaviest in samples from the snow cone and the top of the stalagmite. In contrast, samples from the deepest part of the cave are ~2‰ more depleted. Given local relationships between stable isotopic composition and air temperature, this difference corresponds to a change of ~2 °C. Given that the older samples were deposited ca. A.D. 1700 according to the Bayesian age model, these values provide a minimum estimate of the magnitude of cooling associated with the Little Ice Age in this region. Furthermore, a set of contiguous samples that accumulated over several decades in the early 1700s demonstrates a steady decrease in $\delta^{18}O$ over time, consistent with cooling toward the Little Ice Age maximum.

Glaciochemistry provides information about precipitation chemistry and possibly dust deposition over time. Ca is the most abundant element in the ice, followed by Na, Mg, and K. These same four elements are also present in snow samples collected at nearby monitoring sites. Most of the elements abundant in Strickler Cavern ice were also detectable in a similar glaciochemistry study of a cave in Croatia. On the other hand, Ba, Ni, and Ti were only detected in Strickler Cavern. PCA revealed a group of elements likely related to the local bedrock, a second group reflecting regional transport of mineral dust, and a third group suggestive of eolian transport from an anthropogenic (mining) dust source. Most detectable elements increased in abundance in layers of the stalagmite deposited between A.D. 630 and A.D. 1190 at the same time as ratios of elements representing different principal components changed, suggesting a shift in the balance between snow and dust deposition.

Given the paucity of detailed studies of cave ice from North America, these results constitute a notable step forward in our understanding of these potentially significant paleoenvironmental archives. Future work should build upon the foundation provided by this study to further exploit the significant paleoenvironmental information archived in Strickler Cavern.

**ACKNOWLEDGMENTS**

Permission to work in Strickler Cavern was granted by the U.S. Department of Agriculture Salmon-Challis National Forest in 2015 under Operating Plan CHL62. Thanks go to Gail Baer, Amanda Kriwox, and Katie Wood for their help in coordinating the permitting process. This project was supported by a grant from the American Philosophical Society that was matched by Middlebury College. Radiocarbon dating at the William M. Keck Carbon Cycle Accelerator Mass Spectrometry Laboratory would not have been possible without the support of John Southon and Chanda Bertrand. Thanks also go to Aurel Perşoiu for conducting the stable isotope analyses and Pete Ryan for help with the glaciochemistry. Development of the research plan benefited greatly from conversations with Zoltán Kern, Aurel Perşoiu, and Christoph Spötl. Thanks are extended to David Naftz and an anonymous reviewer for incisive reviews that improved the manuscript.

**REFERENCES CITED**

Abbott, P.M., and Davies, S.M., 2012, Volcanism and the Greenland ice-cores: The tephra record: Earth-Science Reviews, v. 115, p. 173–191, doi:10.1016/j.earscirev.2012.09.001.

Balch, E.S., 1900, Glacieres, or Freezing Caverns: Philadelphia, Allen Lane & Scott, 366 p.

Behm, M., and Hausmann, H., 2007, Eisdickenmessungen in alpinen Höhlen mit Georadar: Die Höhle, v. 58, p. 3–11.

Benjamin, L., Knobel, L.L., Hall, L.F., Cecil, Ld., and Green, J.R., 2005, Development of a local meteoric water line for southeastern Idaho, western Wyoming, and south-central Montana: http://pubs.usgs.gov/sir/2004/5126/ (accessed January 2017).

Bowen, G.J., and Revenaugh, J., 2003, Interpolating the isotopic composition of modern meteoric precipitation: Water Resources Research, v. 39, 1299, doi:10.1029/2003WR002086.

Bowen, G.J., and Wilkinson, B., 2002, Spatial distribution of $\delta^{18}O$ in meteoric precipitation: Geology, v. 30, p. 315–318, doi:10.1130/0091-7613(2002)030<0315:SDOOIM>2.0.CO;2.

Cecil, L.D., Plummer, M., Peters, P., Herron, D.A., Green, J.R., Lords, D., Shuster, P.F., Dewild, J.F., and Krabbenhoft, D.P., 2004, Ice-core research in a cave environment in the Salmon-Challis National Forest, Idaho: Geological Society of America Abstracts with Programs, v. 36, p. 13, https://gsa.confex.com/gsa/2004RM/finalprogram/abstract_72348.htm (accessed November 2016).

Cheng, H., Edwards, R.L., Shen, C.-C., Polyak, V.J., Asmerom, Y., Woodhead, J., Hellstrom, J., Wang, Y., Kong, X., Spötl, C., et al., 2013, Improvements in 230 Th dating, 230 Th and 234 U half-life values, and U-Th isotopic measurements by multi-collector inductively coupled plasma mass spectrometry: Earth and Planetary Science Letters, v. 371, p. 82–91, doi:10.1016/j.epsl.2013.04.006.

Colucci, R.R., Fontana, D., Forte, E., Potleca, M., and Guglielmin, M., 2016, Response of ice caves to weather extremes in the southeastern Alps, Europe: Geomorphology, v. 261, p. 1–11, doi:10.1016/j.geomorph.2016.02.017.

Craig, H., 1961, Isotopic variations in meteoric waters: Science, v. 133, p. 1702–1703, doi:10.1126/science.133.3465.1702.

Dansgaard, W., 1964, Stable isotopes in precipitation: Tellus, v. 16, p. 436–468, doi:10.3402/tellusa.v16i4.8993.

Dickfoss, P.V., Betancourt, J.L., Thompson, L.G., Turner, R.M., and Tharnstrom, S., 1997, History of Ice at Candelaria Ice Cave, New Mexico: New Mexico Bureau of Mines and Mineral Resources Bulletin 156, p. 91–112.

Feurdean, A., Perşoiu, A., Pazdur, A., and Onac, B.P., 2011, Evaluating the palaeoecological potential of pollen recovered from ice in caves: A case study from Scărişoara Ice Cave, Romania: Review of Palaeobotany and Palynology, v. 165, p. 1–10, doi:10.1016/j.revpalbo.2011.01.007.

Foster, D., Brocklehurst, S.H., and Gawthorpe, R.L., 2008, Small valley glaciers and the effectiveness of the glacial buzzsaw in the northern Basin and Range, USA: Geomorphology, v. 102, p. 624–639, doi:10.1016/j.geomorph.2008.06.009.

Froehlich, K., Gibson, J.J., and Aggarwal, P., 2001, Deuterium excess in precipitation and its climatological significance, in Study of Environmental Change using Isotope Techniques: International Atomic Energy Agency C&S Papers 13, p. 54–66.

Fuhrmann, K., 2007, Monitoring the disappearance of a perennial ice deposit in Merrill Cave: Journal of Caves and Karst Studies, v. 69, p. 256–265.

Grootes, P.M., Stuiver, M., White, J.W.C., Johnsen, S., and Jouzel, J., 1993, Comparison of oxygen isotope records from the GISP2 and GRIP Greenland ice cores: Nature, v. 366, p. 552–554, doi:10.1038/366552a0.

Grove, J.M., 2004, Little Ice Ages; Ancient and Modern: London, UK, Routledge, Book, Whole, 718 p., http://search.proquest.com/docview/50432410?accountid=12447.

Haeberli, W., Cihlar, J., and Barry, R.G., 2000, Glacier monitoring within the global climate observing system: Annals of Glaciology, v. 31, p. 241–246, doi:10.3189/172756400781820192.

Hausmann, H., and Behm, M., 2010, Application of ground penetrating radar (GPR) in Alpine ice caves: The Cryosphere Discuss, v. 4, p. 1365–1389, doi:10.5194/tcd-4-1365-2010.

Jouzel, J., and Souchez, R.A., 1982, Melting-refreezing at the glacier sole and the isotopic composition of the ice: Journal of Glaciology, v. 28, p. 35–42, doi:10.1017/S0022143000011771.

Jouzel, J., Masson-Delmotte, V., Cattani, O., Dreyfus, G., Falourd, S., Hoffmann, G., Minster, B., Nouet, J., Barnola, J.M., Chappellaz, J., Fischer, H., Gallet, J.C., Johnsen, S., Leuenberger, M., et al., 2007, Orbital and millennial Antarctic climate variability over the past 800,000 years: Science, v. 317, p. 793–796, doi:10.1126/science.1141038.

Kern, Z., and Perşoiu, A., 2013, Cave ice—The imminent loss of untapped mid-latitude cryospheric palaeoenvironmental archives: Quaternary Science Reviews, v. 67, p. 1–7, doi:10.1016/j.quascirev.2013.01.008.

Kern, Z., and Thomas, S., 2014, Ice level changes from seasonal to decadal time-scales observed in lava tubes, Lava Beds National Monument, NE California, USA: Geografia Fisica e Dinamica Quaternaria, v. 37, p. 151–162.

Kern, Z., Molnár, M., Svingor, É., Perşoiu, A., and Nagy, B., 2009, High-resolution, well-preserved tritium record in the ice of Bortig ice cave, Bihor Mountains, Romania: The Holocene, v. 19, p. 729–736, doi:10.1177/0959683609105296.

Kern, Z., Fórizs, I., Pavuza, R., Molnár, M., and Nagy, B., 2011a, Isotope hydrological studies of the perennial ice deposit of Saarhalle, Mammuthöhle, Dachstein Mts., Austria: The Cryosphere, v. 5, p. 291–298, doi:10.5194/tc-5-291-2011.

Kern, Z., Széles, E., Horvatinčić, N., Fórizs, I., Bočić, N., and Nagy, B., 2011b, Glaciochemical investigations of the ice deposit of Vukuąić ice cave, Velebit Mountain, Croatia: The Cryosphere, v. 5, p. 485–494, doi:10.5194/tc-5-485-2011.

Lauriol, B., and Clark, I.D., 1993, An approach to determine the origin and age of massive ice blockages in two Arctic caves: Permafrost and Periglacial Processes, v. 4, p. 77–85, doi:10.1002/ppp.3430040107.

Laursen, L., 2010, Climate scientists shine light on cave ice: Science, v. 329, p. 746–747, doi:10.1126/science.329.5993.746.

Lechler, A.R., and Niemi, N.A., 2011, The influence of snow sublimation on the isotopic composition of spring and surface waters in the southwestern United States: Implications for stable isotope–based paleoaltimetry and hydrologic studies: Geological Society of America Bulletin, v. 123, p. 318–334, doi:10.1130/B30467.1.

Luetscher, M., 2013, Glacial processes in caves, in Shroder, J., and Frumkin, A., eds., Treatise on Geomorphology: Volume 6. Karst Geomorphology: San Diego, California, Academic Press, p. 258–266.

Luetscher, M., and Jeannin, P.-Y., 2004, A process-based classification of alpine ice caves: Theoretical and Applied Karstology, v. 17, p. 5–10.

Luetscher, M., Jeannin, P.-Y., and Haeberli, W., 2005, Ice caves as an indicator of winter climate evolution: A case study from the Jura Mountains: The Holocene, v. 15, p. 982–993, doi:10.1191/0959683605hl872ra.

Luetscher, M., Bolius, D., Schwikowski, M., Schotterer, U., and Smart, P.L., 2007, Comparison of techniques for dating of subsurface ice from Monlesi ice cave, Switzerland: Journal of Glaciology, v. 53, p. 374–384, doi:10.3189/002214307783258503.

MacDonald, W.D., 1994, Stable isotope composition of cave ice in western North America: Committee on Resources and the Environment, University of Calgary, http://prism.ucalgary.ca/handle/1880/30220 (accessed January 2017).

Mapel, W.J., Reed, W., and Smith, R.K., 1965, Geologic Map and Sections of the Doublespring Quadrangle, Custer and Lemhi Counties, Idaho: U.S. Geological Survey Geological Quadrangle Map GQ-464, scale 1:62,500.

Marshall, P., and Brown, M.C., 1974, Ice in Coulthard Cave, Alberta: Canadian Journal of Earth Sciences, v. 11, p. 510–518, doi:10.1139/e74-045.

May, B., Spötl, C., Wagenbach, D., Dublyansky, Y., and Liebl, J., 2011, First investigations of an ice core from Eisriesenwelt cave (Austria): The Cryosphere, v. 5, p. 81–93, doi:10.5194/tc-5-81-2011.

Moser, H., and Stichler, W., 1974, Deuterium and oxygen-18 contents as an index of the properties of snow covers, in Snow Mechanics: Proceedings of the Grindelwald Symposium: International Association of Hydrological Sciences Publication 114, p. 122–135.

Munroe, J.S., 2014, Properties of modern dust accumulating in the Uinta Mountains, Utah, USA, and implications for the regional dust system of the Rocky Mountains: Earth Surface Processes and Landforms, v. 39, p. 1979–1988, doi:10.1002/esp.3608.

Munroe, J.S., Crocker, T.A., Giesche, A.M., Rahlson, L.E., Duran, L.T., Bigl, M.F., and Laabs, B.J.C., 2012, A lacustrine-based Neoglacial record for Glacier National Park, Montana, USA: Quaternary Science Reviews, v. 53, p. 39–54, doi:10.1016/j.quascirev.2012.08.005.

Munroe, J.S., Klem, C.M., and Bigl, M.F., 2013, A lacustrine sedimentary record of Holocene periglacial activity from the Uinta Mountains, Utah, U.S.A.: Quaternary Research, v. 79, p. 101–109.

Munroe, J.S., Attwood, E.C., O'Keefe, S.S., and Quackenbush, P.J., 2015, Eolian deposition in the alpine zone of the Uinta Mountains, Utah, USA: Catena, v. 124, p. 119–129, doi:10.1016/j.catena.2014.09.008.

Naftz, D.L., and Smith, M.E., 1993, Ice thickness, ablation, and other glaciological measurements on Upper Fremont Glacier, Wyoming: Physical Geography, v. 14, p. 404–414.

Naftz, D.L., Susong, D.D., Schuster, P.F., Cecil, L.D., Dettinger, M.D., Michel, R.L., and Kendall, C., 2002, Ice core evidence of rapid air temperature increases since 1960 in alpine areas of the Wind River Range, Wyoming, United States: Journal of Geophysical Research, ser. D, Atmospheres, v. 107, no. D13, p. ACL 3-1–ACL 3-16, doi:10.1029/2001JD000621.

Perşoiu, A., and Onac, B.P., 2012, Ice in caves, in White, W.B., and Culver, D.C., eds., Encyclopedia of Caves (2nd ed.): Amsterdam, Netherlands, Academic Press, p. 399–404, doi:10.1016/B978-0-12-383832-2.00056-6.

Perşoiu, A., Onac, B.P., Wynn, J.G., Bojar, A.V., and Holmgren, K., 2011, Stable isotope behavior during cave ice formation by water freezing in Scărişoara ice cave, Romania: Journal of Geophysical Research, ser. D, Atmospheres, v. 116, no. D2, D02111, doi:10.1029/2010JD014477.

Petit, J.R., Jouzel, J., Raynaud, D., Barkov, N.I., Barnola, J.-M., Basile, I., Bender, M., Chappellaz, J., Davis, M., Delaygue, G., Delmotte, M., Kotiyakov, V.M., Legrand, M., Lipenkov, V.Y., et al., 1999, Climate and atmospheric history of the past 420,000 years from the Vostok ice core, Antarctica: Nature, v. 399, p. 429–436, doi:10.1038/20859.

Pflitsch, A., Schörghofer, N., Smith, S.M., and Holmgren, D., 2016, Massive ice loss from the Mauna Loa ice cave, Hawaii: Arctic, Antarctic, and Alpine Research, v. 48, p. 33–43, doi:10.1657/AAAR0014-095.

Power, M.J., Marlon, J., Ortiz, N., Bartlein, P.J., Harrison, S.P., Mayle, F.E., Ballouche, A., Bradshaw, R.H., Carcaillet, C., Cordova, C., et al., 2008, Changes in fire regimes

since the Last Glacial Maximum: An assessment based on a global synthesis and analysis of charcoal data: Climate Dynamics, v. 30, p. 887–907, doi:10.1007/s00382-007-0334-x.

Ramsey, C.B., 2009, Bayesian analysis of radiocarbon dates: Radiocarbon, v. 5, no. 1, p. 337–360.

Reasoner, M.A., and Jodry, M.A., 2000, Rapid response of alpine timberline vegetation to the Younger Dryas climate oscillation in the Colorado Rocky Mountains, USA: Geology, v. 28, p. 51–54, doi:10.1130/0091-7613(2000)28<51:RROATV>2.0.CO;2.

Reimer, P.J., Bard, E., Bayliss, A., Beck, J.W., Blackwell, P.G., Ramsey, C.B., Buck, C.E., Cheng, H., Edwards, R.L., Friedrich, M., et al., 2013, IntCal13 and Marine13 radiocarbon age calibration curves 0–50,000 years cal BP: Radiocarbon, v. 55, p. 1869–1887, doi:10.2458/azu_js_rc.55.16947.

Reynolds, R.L., Goldstein, H.L., Moskowitz, B.M., Bryant, A.C., Skiles, S.M., Kokaly, R.F., Flagg, C.B., Yauk, K., Berquó, T., and Breit, G., 2013, Composition of dust deposited to snow cover in the Wasatch Range (Utah, USA): Controls on radiative properties of snow cover and comparison to some dust-source sediments: Aeolian Research, v. 15, p. 73–90, doi:10.1016/j.aeolia.2013.08.001.

Romanovsky, V.E., Smith, S.L., and Christiansen, H.H., 2010, Permafrost thermal state in the polar Northern Hemisphere during the international polar year 2007–2009: A synthesis: Permafrost and Periglacial Processes, v. 21, p. 106–116, doi:10.1002/ppp.689.

Schirrmeister, L., Froese, D., Tumskoy, V., Grosse, G., and Wetterich, S., 2013, Yedoma: Late Pleistocene ice-rich syngenetic permafrost of Beringia, in Elias, S., ed., Encyclopedia of Quaternary Science (2nd ed.): Amsterdam, Netherlands, Elsevier, p. 542–552.

Schöner, W., Weyss, G., and Mursch-Radlgruber, E., 2011, Linkage of cave-ice changes to weather patterns inside and outside the cave Eisriesenwelt (Tennengebirge, Austria): The Cryosphere, v. 5, p. 603–616, doi:10.5194/tc-5-603-2011.

Schuster, P.F., White, D.E., Naftz, D.L., and Cecil, L.D., 2000, Chronological refinement of an ice core record at Upper Fremont Glacier in south central North America: Journal of Geophysical Research, ser. D, Atmospheres, v. 105, p. 4657–4666, doi:10.1029/1999JD901095.

Serreze, M.C., Holland, M.M., and Stroeve, J., 2007, Perspectives on the Arctic's shrinking sea-ice cover: Science, v. 315, p. 1533–1536.

Souchez, R.A., and Jouzel, J., 1984, On the isotopic composition in δD and $\delta^{18}O$ of water and ice during freezing: Journal of Glaciology, v. 30, p. 369–372, doi:10.1017/S0022143000006249.

Spötl, C., Reimer, P.J., and Luetscher, M., 2014, Long-term mass balance of perennial firn and ice in an Alpine cave (Austria): Constraints from radiocarbon-dated wood fragments: The Holocene, v. 24, p. 165–175, doi:10.1177/0959683613515729.

Stichler, W., Schotterer, U., Fröhlich, K., Ginot, P., Kull, C., Gäggeler, H., and Pouyaud, B., 2001, Influence of sublimation on stable isotope records recovered from high-altitude glaciers in the tropical Andes: Journal of Geophysical Research, v. 106, p. 22,613–22,620, doi:10.1029/2001JD900179.

Stoffel, M., Luetscher, M., Bollschweiler, M., and Schlatter, F., 2009, Evidence of NAO control on subsurface ice accumulation in a 1200 yr old cave-ice sequence, St. Livres ice cave, Switzerland: Quaternary Research, v. 72, p. 16–26, doi:10.1016/j.yqres.2009.03.002.

Summerhayes, C.P., 2008, International collaboration in Antarctica: The international polar years, the international geophysical year, and the scientific committee on Antarctic research: The Polar Record, v. 44, p. 321–334, doi:10.1017/S0032247408007468.

Vandenberghe, J., 2013, Grain size of fine-grained windblown sediment: A powerful proxy for process identification: Earth-Science Reviews, v. 121, p. 18–30, doi:10.1016/j.earscirev.2013.03.001.

Veni, G., Land, L., and Perşoiu, A., 2014, Time, money, and melting ice: Proposal for a cooperative study of the world's cave ice in a race against climate change: The International Workshop on Ice Caves, http://scholarcommons.usf.edu/iwic/Proceedings/Climate_Microclimates_Cave_Ice/1 (last accessed 30 June 2017).

Wahr, J., Wingham, D., and Bentley, C., 2000, A method of combining ICESat and GRACE satellite data to constrain Antarctic mass balance: Journal of Geophysical Research–Solid Earth, v. 105, p. 16,279–16,294, doi:10.1029/2000JB900113.

Wilson, A.B., and Skipp, B.A., 1994, Geologic Map of the Eastern Part of the Challis National Forest and Vicinity, Idaho: https://pubs.er.usgs.gov/publication/i2395 (accessed November 2016).

Yonge, C.J., 2014, Stable isotope composition of perennial ice in caves as an aid to characterizing ice cave types: The International Workshop on Ice Caves, http://scholarcommons.usf.edu/iwic/Proceedings/Ice_Cave_Processes/9/ (accessed January 2017).

Yonge, C.J., and MacDonald, W.D., 1999, The potential of perennial cave ice in isotope palaeoclimatology: Boreas, v. 28, p. 357–362, doi:10.1080/030094899422082.

Žák, K., Onac, B.P., and Peşoiu, A., 2008, Cryogenic carbonates in cave environments: A review: Quaternary International, v. 187, p. 84–96, doi:10.1016/j.quaint.2007.02.022.

Science Editor: Bradley S. Singer
Associate Editor: Joan Florsheim

Manuscript Received 20 February 2017
Revised Manuscript Received 7 May 2017
Manuscript Accepted 1 July 2017

Printed in the USA